

INTERIM  
111-75-CR  
8482  
37P

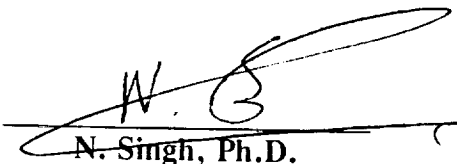
NASA-CR-195820

THE UNIVERSITY OF ALABAMA IN HUNTSVILLE  
UAH RESEARCH PROPOSAL 94-429

# IONOSPHERIC PLASMA OUTFLOW IN RESPONSE TO TRANSVERSE ION HEATING: SELF-CONSISTENT MACROSCOPIC TREATMENT

Third year funding request  
and  
annual report  
for  
**NAGW-2903**

Prepared by



N. Singh, Ph.D.

Principal Investigator

Department of Electrical and Computer Engineering  
The University of Alabama in Huntsville  
Huntsville, AL 35899  
205-895-6678

Submitted by

The University of Alabama in Huntsville



Sue B. Weir

Research Administrator

May 1994

N94-33048

Unclass

G3/75 0008482

(NASA-CR-195820) IONOSPHERIC  
PLASMA OUTFLOW IN RESPONSE TO  
TRANSVERSE ION HEATING:  
SELF-CONSISTENT MACROSCOPIC  
TREATMENT Annual Progress Report  
No. 3, 1993 - 1994 (Alabama Univ.)  
37 p



# **Ionospheric Plasma Outflow in Response to Transverse Ion Heating: Self-Consistent Macroscopic Treatment**

Grant # NAGW-2903, NASA/Headquarters

P. I.: Dr. N. Singh

## **Brief Summary of Work Performed Since July 1, 1993:**

In the previous grant year we examined the effect of transverse ion heating on the polar wind outflow using both a hydrodynamic model [Singh, 1992] and a semikinetic, small-scale simulation model [Singh and Chan, 1993]. These studies demonstrated that the transverse ion heating creates significant plasma perturbations in the polar wind; the perturbation consists of (1) plasma cavity formation for extended heating, (2) formation of a density depletion and an enhancement on its top in response to a localized heating, (3) generation of upward pointing electric fields like in a double layer in response to a localized heating, and (4) generation of waves by the ion-ion instability.

The direct observational evidence of the cavity formation in response to the transverse heating came from recent rocket experiments called TOPAZ I and III. The experiments revealed that filamentary cavities, with depletions as high as 80% and aligned with the Earth's magnetic field, occur at altitudes  $\sim 10^3 km$ . These cavities were observed in conjunction with intense lower hybrid waves and transversely heated ions [Kinter et al, 1992]. As the rocket cut across the filamentary plasma cavities with width  $\sim 50 m$ , the waves appear as spikes with a duration of 50 ms. The original interpretation of the cavity formation was given in terms of lower hybrid wave collapse [Vago et al, 1992].

We examined the various likely processes for creating the cavities and found that the mirror force acting on the transversely heated ions is the most likely mechanism [Singh, 1994; Singh and Chan, 1993]. The pondermotive force causing the wave collapse was found to be a much weaker force than the mirror force on the transversely heated ions observed inside the cavities along with the lower hybrid waves.

Using a hydrodynamic model for the polar wind we modeled the cavity formation and found that for the heating rate obtained from the observed waves, the mirror force does create cavities with depletions as observed. Some initial results from this study were published in a recent Geophysical Research Letters [Singh, 1994] and were reported in the Fall AGU meeting in San Francisco. We have continued this investigation using a large-scale semikinetic model.



We have also continued our investigation on the microprocesses driven by the transverse ion heating [Singh and Chan, 1993]. In the previous study we performed simulations using a small-scale semikinetic code. We have extended this code to be fully kinetic by treating both electrons and ions kinetically. The goal of this study is to examine how the process of the transverse ion heating energizes electrons parallel to the magnetic field as observed from satellites.

### **Tasks for the Grant Period Beginning July 1, 1994:**

We will continue to study the microprocesses responsible for the transfer of energy from the transversely heated ions to the electrons. During the present grant period we developed the code. We plan to perform a systematic set of simulation runs and analyze them theoretically.

We will also continue to study the process of the cavity formation by the lower hybrid waves, which has been now observed from satellites as well [Holback et al, 1993]. Using the semikinetic modeling we plan to examine the issue of bulk versus tail heating of the ions. When the lower hybrid waves are relatively slow they affect the entire velocity distribution function of the polar wind ions. On the other hand, for relatively fast waves only a tail heating is likely. In the former case a strong density depletion occurs, while in the latter case only weak depletions are possible. A systematic theoretical study of this type comparing the results from the modeling and the observations will greatly improve our understanding of the filamentary cavities observed in the auroral region.

### **Publications Under Grant # NAGW-2903**

1. N. Singh, Ponderomotive versus mirror force in creation of the filamentary cavities in auroral plasma, *Geophys. Res. Lett.*, 21, 257, 1994.
2. N. Singh and C. B. Chan, Numerical simulation of plasma processes driven by transverse ion heating, *J. Geophys. Res.*, 98, 11,677, 1993.
3. C. W. Ho, J. R. Horwitz, N. Singh and G. R. Wilson, Plasma expansion and evolution of density perturbations in the polar wind: Comparison of semi-kinetic and transport models, *J. Geophys. Res.*, 98, 13,581, 1993.
4. N. Singh, Cavitons or simply plasma depletions by transverse ion heating, *EOS*, 74, 532, 1993. 1993 Fall Meeting, Dec. 7-11. 1993, San Francisco.



## References

- Holback, B. R. Bostrom, A. I. Ericksson, P. O. Dovner, and G. Holmgren, Characteristics of spikelets seen from Freja, *EOS*, 74, 526, 1993.
- Kinter, P. M., J. Vago, S. Chesney, R. L. Arnoldy, K. A. Lynch, C. J. Pollock, and T. E. Moore, *Phys. Rev. Lett.*, 68, 2448, 1992.
- Singh, N., Plasma perturbations created by transverse ion heating events in the magnetosphere, *J. Geophys. Res.*, 97, 4235, 1992.
- Vago, J. L., P. M. Kinter, S. W. Chesney, R. L. Arnoldy, K. A. Lynch, T. E. Moore, and C. J. Pollock, Transverse ion acceleration by localized lower-hybrid waves in the topside auroral ionosphere, *J. Geophys. Res.*, 97, 16,935, 1992





THE UNIVERSITY OF ALABAMA IN HUNTSVILLE  
 UAH RESEARCH PROPOSAL 94-429  
 COST ESTIMATE FOR A ONE-YEAR PERIOD  
 (July 1, 1994 - June 30, 1995)

Third year funding for NAGW-2903

		FY'94	FY'95	TOTAL
		7/1/94-9/30/94	10/1/94-6/30/95	
<b>A. SALARIES AND WAGES</b>				
	/1/			
1. Dr. N. Singh, Principal Investigator *				
	16% x 7 weeks x \$1,589.74/wk.	1,781		
	16% x 6 weeks x \$1,675.68/wk.	1,609		
	16% x 31 weeks x \$1,742.70/wk.		8,644	
	16% x 7 weeks x \$1,742.70/wk.		1,952	13,985
2. Secretary				
	5% x 3/12 yr. x \$18,889	236		
	5% x 9/12 yr. x \$19,645		737	973
3. Undergraduate Research Assistant				
	10 hr. wk. @ \$5.20/hr.	676	1,976	2,652
TOTAL SALARIES AND WAGES		4,301	13,308	17,610
<b>B. FRINGE BENEFITS (21% A.1. &amp; A.2.)</b>				
	/2/	761	2,380	3,141
<b>C. OPERATING COSTS</b>				
1. Supplies, reproduction		75	220	295
2. Page charges		0	850	850
TOTAL OPERATING COSTS		75	1,070	1,145
<b>D. TRAVEL</b>				
	/3/			
1. See below		0	1,280	1,280
TOTAL DIRECT COST		5,138	18,038	23,176
<b>E. INDIRECT</b>				
	/4/			
1. 42.0% MTDC		2,158	0	2,158
2. 42.5% MTDC		0	7,666	7,666
TOTAL INDIRECT		2,158	7,666	9,824
<b>TOTAL ESTIMATED COST</b>		7,295	25,704	<b>\$33,000</b>

\* UAH changes from a quarter to semester academic year beginning 8/19/94. This change affects the way an academic appointment's time is computed. UAH's annual merit increase occurs on October 1. The four components of Dr. Singh's salary listed above are:

7 weeks of summer 1994 (7/1/94-8/18/94) figured on the weekly rate of an FY'94 academic year (39 weeks) base of \$62,000 (\$62,000/39)

6 weeks of academic year 1995 (8/19/94-9/30/95) figured on the weekly rate of the new semester academic year (37 weeks) from the \$62,000 base. (\$62,000/37)

31 weeks of the remainder of the 1995 academic year figured on the new base of \$64,480 (4% increase) (\$64,480/37)

7 weeks of summer 1995 (May 15-June 30) at same weekly rate as academic year 1995

D.1. Travel to professional meeting to present paper/Washington, DC used for estimation purposes = \$1,280  
 air fare = \$623 (travel agent quote), per diem = \$144 x 3 days (GSA rate), registration = \$125, misc. = \$50

/1/ See paragraph 2.a. of financial data sheet

/2/ See paragraph 2.b. of financial data sheet

/3/ See paragraph 2.c. of financial data sheet

/4/ See paragraph 2.d. of financial data sheet



# FINANCIAL DATA SHEET

## 1. Price Summary

The cost estimate presents applicable pricing information in the standard format adopted by the University.

## 2. Cost Substantiation

### a. Salaries:

Proposed salaries are quoted as actuals and are increased by 4.0 percent each fiscal year to cover anticipated raises. These increases are MERIT, not cost-of-living, raises. Percentage of time is estimated. Salaries are verifiable through the established payroll system and after-the-fact certification of effort.

### b. Fringe benefits:

Paid absences such as vacation, sick leave, and holidays are included in salaries and are charged as a direct expense as negotiated in the indirect rate.

Fringe benefits are charged as a direct expense. They include State Teachers' Retirement, Teachers' Insurance and Annuity Association--The College Retirement Equities Fund, social security, disability insurance, and life insurance where applicable. Graduate Research Assistants receive tuition assistance as a fringe benefit in lieu of salary.

### c. Travel:

Reimbursement of travel will be in accordance with The University of Alabama travel regulations. Expenses for out-of-state travel will be paid on the basis of actual, reasonable, and necessary expenses. Expenses for in-state travel will be paid on a per diem basis. Transportation costs will be reimbursed on the basis of actual costs for common carrier and at the approved rate per mile for automobiles.

### d. Indirect Rate:

The University negotiates its pre-determined indirect rate with the Department of Health and Human Services. The provisional (in negotiation) indirect rates are as follows:

	FY'94	FY'95	FY'96	FY'97		FY'94	FY'95	FY'96	FY'97
On-campus Research	42.0%	42.5%	43.0%	43.0%	Off-campus Research	26.0%	26.0%	26.0%	26.0%
On-campus Instruction	62.6%				Off-campus Instruc.	25.9%			
On-campus Public Service	39.4%				Off-campus Pub. Ser.	26.0%			

These rates are based on Modified Total Direct Costs (MTDC). Indirect is not charged on capital expenditures such as equipment, alterations, and renovations. Only the first \$25,000 of each subcontract is subject to indirect rates and participant support costs to not incur indirect.

### e. Approved Procurement System:

The UAH procurement system has been approved by the Department of the Navy, Office of Naval Research, through September 30, 1994.

## 3. Government Agency Contacts:

Administrative Contracting Officer :  
 Office of Naval Research Resident Representative  
 Atlanta Area Office  
 101 Marietta Tower  
 Suite 2805  
 Atlanta, GA 30303  
 ATTN: Charles K. Hayes (NASA awards)  
 404-730-9255  
 ATTN: Kathy L. Raible (All other awards)  
 407-730-9262

Audit Functions:  
 DHHS/OIG  
 Office of Audit  
 Federal Building  
 P.O. Box 1704  
 Atlanta, GA 30301  
 ATTN: Michael D. Geiger, Audit Mgr.  
 404-331-2446

## 4. Awards:

Resulting contracts or grants should be forwarded to:

**Research Administration**  
**The University of Alabama in Huntsville**  
**Research Institute/Room E-39**  
**Huntsville, AL 35899**  
**205-895-6000; 205-895-6677 (fax)**



**CERTIFICATION REGARDING DRUG-FREE REQUIREMENTS  
(Grants/Cooperative Agreements)**

A. The grantee certifies that it will provide a drug-free workplace by:

1. Publishing a statement notifying employees that the unlawful manufacture, distribution, dispensing, possession or use of a controlled substance is prohibited in the grantee's workplace and specifying the actions that will be taken against employees for violations of such prohibition:

2. Establishing a drug-free awareness program to inform employees about:

- (a.) The dangers of drug abuse in the workplace;
- (b.) The grantee's policy of maintaining a drug-free workplace;
- (c.) Any available drug counseling, rehabilitation, and employee assistance programs;
- (d.) The penalties that may be imposed upon employees for drug abuse violations occurring in the workplace.

3. Making it a requirement that each employee to be engaged in the performance of the grant be given a copy of the statement required by paragraph 1.

4. Notifying the employee in the statement required by paragraph 1 that, as a condition of employment under the grant, the employee will:

- (a.) Abide by the terms of the statement, and
- (b.) Notify the employer of any criminal drug statute conviction for a violation occurring in the workplace no later than five days after such conviction.

5. Notifying the agency within ten days after receiving notice under subparagraph 4(b), with respect to any employee who is so convicted.

6. Taking one of the following actions, within 30 days of receiving notice under subparagraph 4(b), with respect to any employee who is so convicted:

- (a.) Taking appropriate personnel action against such an employee, up to and including termination, or
- (b.) Requiring such employee to participate satisfactorily in a drug abuse or rehabilitation program approved for such purposes by a Federal, State or local health, law enforcement, or other appropriate agency.

7. Making a good faith effort to continue to maintain a drug-free workplace through implementation of paragraphs 1, 2, 3, 4, 5, and 6.

B. The grantee shall insert in the space provided below the site(s) for the performance of the work done in connection with specific grant:

**Place of Performance:** The University of Alabama in Huntsville, Huntsville, Madison Co., AL

**Responsible University Official:** Sue B. Weir 5-4-94  
Sue B. Weir, Research Administrator Date

**Title/Identification of Applicable Research Proposal:** UAH Proposal 94-429



**CERTIFICATION REGARDING DEBARMENT, SUSPENSION, AND  
OTHER RESPONSIBILITY MATTERS --  
PRIMARY COVERED TRANSACTIONS**

(1.) The prospective primary participant certifies that, to the best of its knowledge and belief, it and its principals:

(a.) Are not presently debarred, suspended, proposed for debarment, declared ineligible, or voluntarily excluded from covered transactions by any Federal department or agency.

(b.) Have not within a three-year period preceding this proposal been convicted or had a civil judgment rendered against them for commission of fraud performing a public (Federal, State or local) transaction or contract under a public transaction; violation, theft, forgery, bribery, falsification or destruction of records, making false statements, or receiving stolen property.

(c.) Are not presently indicted or otherwise criminally or civilly charged by a government entity (Federal, State, or local) with commission of any of the offenses enumerated in paragraph (1.) (b.) of this certification; and

(d.) Have not within a three-year period preceding this application/proposal had one or more public transactions (Federal, State, or local) terminated for cause or default.

(2.) Where the prospective primary participant is unable to certify to any of the statements in this certification, such prospective participant shall attach an explanation to this proposal

**Proposal identification:** 94-429

**Signature:** Sue B. Weir **Date:** 5-4-94

**Name & Title:** Sue B. Weir, Research Administrator

**Institution:** The University of Alabama in Huntsville





**CERTIFICATION REGARDING LOBBYING  
CONTRACTS, GRANTS, LOANS & COOPERATIVE  
AGREEMENTS**

The undersigned certifies, to the best of his/her knowledge, that:

1. No Federal appropriated funds have been paid or will be paid, by or on behalf of the undersigned, to any person for influencing or attempting to influence an officer or employee of any agency, a Member of Congress, an officer or employee of Congress, or an employee of a Member of Congress in connection with the awarding of any Federal contract, the making of any Federal grant, the making of any Federal loan, the entering into of any cooperative agreement, and the extension, continuation, renewal, amendment, or modification on any Federal contract, grant, loan or cooperative agreement.

2. If any funds other than Federal appropriated funds have been paid or will be paid to any person for influencing or attempting to influence an officer or employee of any agency, a Member of Congress, an officer or employee of Congress, or any employee of a Member of Congress in connection with this Federal contract, grant, loan or cooperative agreement, the undersigned shall complete and submit Standard Form-LLL, "Disclosure Form to Report Lobbying," in accordance with its instructions.

3. The undersigned shall require that the language of this certification be included in the award documents for all subawards at all tiers (including subcontracts, subgrants, and contracts under grants, loans, and cooperative agreements) and that all subrecipients shall certify and disclose accordingly.

This certification is a material representation of fact upon which reliance was placed when this transaction was made or entered into. Submission of this certification is prerequisite for making or entering into imposed by Section 1352, title 31 US. Code Any person who fails to file the required certification shall be subject to a civil penalty of not less than \$10,000 and not more than \$100,000 for each such failure.

The University of Alabama in Huntsville  
Organization Name

UAH Proposal 94-429  
Award Number

Sue B. Weir, Research Administrator  
Name and Title of Authorized Person

\_\_\_\_\_  
Signature

*Sue B. Weir*

*5-4-94*

Date



## Pondermotive versus mirror force in creation of the filamentary cavities in auroral plasma

Nagendra Singh

Department of Electrical and Computer Engineering, The University of Alabama in Huntsville

**Abstract.** Recently rocket observations on spikelets of lower-hybrid waves along with strong density cavities and transversely heated ions were reported. The observed thin filamentary cavities oriented along the magnetic field in the auroral plasma have density depletions up to several tens of percent. These observations have been interpreted in terms of a theory for lower-hybrid wave condensation and collapse. The modulational instability leading to the wave condensation of the lower-hybrid waves yields only weak density perturbations, which cannot explain the above strong density depletions. The wave collapse theory is based on the nonlinear pondermotive force in a homogeneous ambient plasma and the density depletion is determined by the balance between the wave pressure (pondermotive force) and the plasma pressure. In the auroral plasma, the balance is achieved in a time  $\tau_{wc} \leq 1$  ms. It is shown here that the mirror force, acting on the transversely heated ions at a relatively long time scale, is an effective mechanism for creating the strong plasma cavities. We suggest that the process of wave condensation, through the pondermotive force causing generation of short wavelength waves from relatively long wavelength waves, is a dominant process until the former waves evolve and become effective in the transverse heating of ions. As soon as this happens, mirror force on ions becomes an important factor in the creation of the density cavities, which may further trap and enhance the waves. Results from a model of cavity formation by transverse ion heating show that the observed depletions in the density cavities can be produced by the heating rates determined by the observed wave amplitudes near the lower-hybrid frequency. It is found that the creation of a strong density cavity takes a few minutes.

### Introduction

In a recent paper, Vago et al [1992] reported interesting results from rocket (TOPAZ III) observations on lower-hybrid waves and associated heating of ions transverse to the magnetic field lines in the auroral plasma. The rocket observations reveal that intense lower-hybrid waves occur in thin plasma cavities oriented along the geomagnetic field lines. In the cavities, plasma depletions up to 80% have been reported. As the rocket crosses the cavity, the lower-hybrid waves appear as spikelets of 50- to 100-ms duration giving the cavity width 50-100 m across the magnetic field lines. Lower-hybrid wave amplitudes up to 300 mV/m have been reported. The characteristic energy of the transversely heated

ions is reported to be 6 eV. However, the energy spectrograms for the reported spikelet events show acceleration up to ~30 eV [Vago et al, 1992].

Vago et al [1992] have interpreted their observations in terms of the theory for the collapse of lower-hybrid waves [Morales and Lee, 1975; Sotnikov et al, 1978]. According to this theory, the nonlinear pondermotive force associated with the wave expels plasma forming density cavities. In view of the dispersion property of the lower-hybrid wave, the wave number is enhanced in the depletion region. The consequent refraction of the waves into the cavity leads to wave trapping and its intensification, which in turn, intensifies the process of cavity formation. Eventually the wave collapses into a filamentary structure like the observed spikelets. This process can create density depletions of a few percent; the theory of modulational instability operative in this process yields a density perturbation  $\delta n/n \equiv (\omega_{pe}^2 / \Omega_e \omega_{lh}) W / nT$ , where  $\omega_{pe}$ ,  $\Omega_e$ , and  $\omega_{lh}$  are the electron plasma, cyclotron, and lower-hybrid frequencies, respectively;  $W$  is the wave electrostatic energy density and  $nT$  is the thermal energy density of the plasma. For the parameters of the observations  $\delta n/n \sim 4 \times 10^{-2}$ . Therefore there is a difficulty in explaining the observations in terms of the wave collapse involving the pondermotive force alone.

Recently Singh [1992] and Singh and Chan [1993] reported that a natural consequence of transverse ion heating is the formation of a density cavity. For spatially extended bulk heating of ions, the density depletion can be deep and it extends along the magnetic field lines without a significant density enhancement on top of the cavity. On the other hand, for a localized heating the density cavity and enhancement go hand-in-hand. The cavity formation is caused by the plasma expulsion by the upward mirror force acting on the transversely heated ions. Since transversely heated ions are an integral part of the observations, we examine here the relative roles of the mirror and pondermotive forces in the cavity formation.

The question arises here as to which force, the mirror or the pondermotive force or their combined effect, is driving the process of plasma depletion in the observed cavities. The purpose of this letter is to compare these forces for the parameters of the plasma during the observed wave spikelet events [Vago et al, 1992]. We find that in the initial stage of the cavity formation with weaker fields of about 25 mV/m [Vago et al, 1992], even a slight transverse ion heating causes a mirror force exceeding the pondermotive force. Only when the wave field intensifies to values greater than 200 mV/m, the two forces become comparable. In view of this, we suggest that the evolution of the density cavity and the lower-hybrid waves occurs in two stages; in the early stage the long wavelength lower-hybrid waves, probably generated by the auroral electron beams [Vago et al, 1992], undergo a

Copyright 1994 by the American Geophysical Union.

Paper number 93GL03387  
0094-8534/94/93GL-03387\$03.00

modulational instability [Sotnikov et al, 1978; Shapiro et al, 1993] generating waves with shorter and shorter wavelengths until they become effective in transverse heating of ions. For strong waves, such a heating is expected to occur when the difference between the perpendicular wave phase velocity and the wave trapping width becomes comparable to the velocity spread of the thermal ions. As soon as the heating begins to enhance the perpendicular temperature of the ions, the mirror force becomes an important cause for the plasma depletion in the density cavities; the depletions in the cavity can be up to several tens of percent, which cannot be achieved by the pondermotive force alone. Calculations show that the observed amplitude levels of the lower-hybrid waves produce sufficiently strong heating to create density cavities with depletions as observed.

### Comparison of Pondermotive and Mirror Forces

The effects of pondermotive force on the nonlinear evolution of lower-hybrid waves have been studied by including different types of nonlinearities. In the early work of Morales and Lee [1975] the nonlinearity considered arose from the motions of charged particles along the fields of the wave. In later studies [Sotnikov et al, 1978; Shapiro et al, 1993] it was shown that a much stronger nonlinearity arises due to the  $\mathbf{E} \times \mathbf{B}$  drift of the electrons, where  $\mathbf{E}$  is the wave electric field and  $\mathbf{B}$  is the ambient magnetic field. This latter nonlinearity gives rise to a stronger pondermotive force than that given in the early work of Morales and Lee [1975]. The magnitude of the pondermotive force given by Shapiro et al [1993] is

$$F_{e\parallel} = -\frac{1}{2} \frac{\epsilon_0}{n_0} \frac{\omega_{pe}^2}{\Omega_e \omega_{th}} \frac{\partial}{\partial z} |E_{\perp}|^2 \quad (1)$$

where  $F_{e\parallel}$  is the pondermotive force acting on electrons,  $\omega_{pe}$  and  $\Omega_e$  are the electron plasma and cyclotron frequencies, respectively,  $\epsilon_0$  is the permittivity of free space,  $n_0$  is the ambient plasma density, and  $E_{\perp}$  is the wave electric field component perpendicular to the ambient magnetic field.

In order to assess the relative importance of the above pondermotive force and the mirror force acting on transversely heated ions, we compare these two forces. The latter force is given by

$$F_m = -(T_{\perp} - T_{\parallel}) \frac{1}{B} \frac{\partial B}{\partial z} \quad (2)$$

where  $T_{\perp}$  and  $T_{\parallel}$  are, respectively, the perpendicular and parallel ion temperatures in energy units, and  $B(z)$  is the geomagnetic field. Along the auroral flux tubes,  $B(z) = B_0 (R_e / z)^3$ , where  $B_0$  is the magnetic field when the geocentric distance  $z = R_e$ , the Earth's radius. Using this information, (2) can be written as

$$F_m = 3(T_{\perp} - T_{\parallel}) / z \quad (3)$$

It is worthwhile to point out that for an isotropic ion temperature ( $T_{\perp} = T_{\parallel}$ ), mirror force  $F_m = 0$ . When  $T_{\perp} > T_{\parallel}$ , there is an upward force on the ions.

The plasma conditions for the reported spikelet events are as follows [Vago et al, 1992]: plasma density  $n \approx 10^{10} \text{ m}^{-3}$ , electron and ion temperatures  $\sim 5000 \text{ K}$ , electron cyclotron

frequency  $f_{ce} = 10^6 \text{ Hz}$  and the plasma frequency  $f_{pe} \sim 10^6 \text{ Hz}$ . The plasma predominantly consists of  $O^+$  ions at an altitude of about  $10^3 \text{ km}$ . In such a plasma, the lower-hybrid frequency is given by  $\omega_{th} = \omega_{pi} (1 + \omega_{pe}^2 / \Omega_e^2)^{-1/2} \approx 0.7 \omega_{pi}$ , where  $\omega_{pi}$  is the ion-plasma frequency.

For evaluating the pondermotive force  $F_{e\parallel}$ , we need to estimate the parallel scale length in the variation of  $|E_{\perp}(z)|$ . We assume that it is determined by the intimate relationship between the parallel ( $L_{\parallel}$ ) and the perpendicular ( $L_{\perp}$ ) scale lengths of the lower-hybrid waves, namely,

$$L_{\parallel} = (m_i / m_e)^{1/2} L_{\perp} \quad (4)$$

$L_{\parallel}$  is the width of the observed filamentary cavity; for the purpose of calculations we assume  $L_{\perp} \approx 100 \text{ m}$  and find  $L_{\parallel} \approx 17 \text{ km}$ . If the lower-hybrid wave is excited by an auroral electron beam with energy of a few hundred eV, the above values of  $L_{\perp}$  and  $L_{\parallel}$  are about ten times the perpendicular and parallel wavelengths of the wave, respectively. The differential  $\partial / \partial z$  appearing in (1) can be approximated by  $\partial |E_{\perp}|^2 / \partial z \approx |E_{\perp}|^2 / L_{\parallel}$ , which yields

$$F_{e\parallel} \approx 6.3 \times 10^{-24} |E_{\perp}|^2 \text{ N} \quad (5)$$

Taking the nominal value of the electric field  $|E_{\perp}| = 25 \text{ mV/m}$  for the time just before the cavity forms [Vago et al, 1992], we find  $F_{e\parallel} \approx 4 \times 10^{-27} \text{ N}$ . This force is transmitted to ions by an ambipolar electric field if the pondermotive force is the only force acting on the plasma.

At an altitude of  $10^3 \text{ km}$ , the mirror force from (3) is  $F_m \approx 6.5 \times 10^{-26} \Delta T$ , where  $\Delta T = T_{\perp} - T_{\parallel}$ , and it is expressed in eV. Comparing  $F_{e\parallel}$  with  $F_m$ , we find that the latter becomes more effective than the former as soon as ions are transversely heated giving

$$\Delta T > 0.16 \text{ eV} \quad (6)$$

that is, even for a slight perpendicular heating the parallel mirror force begins to dominate the parallel pondermotive force on ions.

It is important to point out that as the pondermotive and the mirror forces act to create the plasma cavity, the electric field is enhanced by wave trapping and the transverse ion temperature is enhanced by the ion heating. Thus the pondermotive and the mirror forces evolve simultaneously. The exact nature of the evolution and their relative importance have not been studied so far. However, we find that even in the late stage of the evolution the mirror force is an important factor. For example, if we assume that in the late stage when the deep cavities have formed,  $E_{\perp} \approx 200 \text{ mV/m}$  and  $\Delta T = 6 \text{ eV}$ ,  $F_{e\parallel} = 2.5 \times 10^{-25} \text{ N}$  and  $F_m = 4 \times 10^{-25} \text{ N}$ .

A major difficulty with the wave collapse theory, based on the nonlinear pondermotive force, is in explaining the observed levels of plasma depletions in the density cavities. This theory predicts that the quasineutral density perturbation in the plasma is given by [Shapiro et al, 1993]

$$\delta n / n_0 \approx \frac{\omega_{pe}^2}{\Omega_e \omega_{th}} \epsilon_0 |E_{\perp}|^2 / 4(T_e + T_i) \quad (7)$$

Assuming  $|E_{\perp}| = 300 \text{ mV/m}$ , the maximum value of the

electric fields reported by Vago et al [1992],  $T_e = T_i = 0.5$  eV and  $n_0 \cong 10^{10} \text{ m}^{-3}$ , we find  $\delta n/n_0 \cong 4 \times 10^{-2}$ , which is at least an order of magnitude smaller than the strong plasma depletions in the observed cavities. The main reason for the weak plasma depletion is that the density perturbations are determined by the balance between the wave pressure (pondermotive force) and the plasma pressure in a homogeneous ambient plasma. The theory of Shapiro et al [1993] shows that the balance is achieved at a time scale  $\tau_{wc} = 0.1 \omega_{pi}^{-1}$ , which is less than a millisecond in the auroral plasma. The subscript "wc" on  $\tau$  refers to the time scale of wave collapse in a homogeneous ambient plasma. However, if the wave collapse has created strong waves effective in heating ions, the continued heating of ions over a relatively long time can create strong cavities. We demonstrate this by a model calculation.

### Modeling of Cavity Formation

In order to demonstrate the effectiveness of the mirror force in creating the cavity with the observed levels of wave amplitude, we adopt a model based on hydrodynamic transport equations for the  $O^+$  ions in the polar wind [Singh, 1992]. Electrons are assumed to obey the Boltzmann law with a temperature of 0.5 eV. The cavity formation and the wave must evolve simultaneously. In this paper we cannot study this simultaneous evolution. However, we can develop a feel for the depth and time constants of the plasma cavity formation by considering plasma depletions by the mirror force for the representative values of the observed wave amplitudes. From Vago et al [1992], we estimate that the power spectral density  $\psi < 10^{-8} \text{ V}^2 \text{ m}^{-2} \text{ Hz}^{-1}$ . Thus, the heating rate is limited to  $\partial T_{\perp} / \partial t < 0.14 \text{ eV/s}$  [Singh and Schunk, 1984]. We calculate the response of the plasma to such a heating in an auroral flux tube by considering different transverse heating rates. We consider a portion of a flux tube from an altitude of 1000 to 2800 km. First a polar wind type of flow consisting of  $O^+$  ions is established in it, with boundary conditions at 1000 km altitude as follows: density  $n_0 = 10^4 \text{ cm}^{-3}$ , equal electron and ion temperatures  $T_0 = 0.5$  eV, and flow velocity  $V_0 = V_{ti}$ , the ion thermal velocity. At the top end of the flux tube we assume the flow is continuous. The perpendicular ion heating is switched on at  $t=0$  for altitudes  $h > 1200$  km. Figures 1a and 1b show the temporal evolution of the density and perpendicular temperature, respectively, in the flux tube for a relatively low heating rate of  $0.014 \text{ eV/s}$ . The temporal evolution up to 3 minutes are shown: At  $t=1$  min., the cavity is quite weak. By the time  $t=3$  min., the cavity has grown to about  $\delta n/n_0 \cong 10\%$  and it extends to an altitude of 2200 km. The corresponding evolution of  $T_{\perp}$  shows a typical feature of extended heating [Singh, 1992]; the temperature increases with the altitude inside the cavity and then it saturates, with saturation value increasing with time. The maximum temperature inside the cavity at  $t=3$  min. is about  $T_{\perp} = 7 T_0 = 3.5$  eV.

Figures 2a and 2b show the evolution of  $n(r)$  and  $T_{\perp}(r)$  for a stronger heating rate of  $0.14 \text{ eV}$  corresponding to  $\psi \cong 10^{-8} \text{ V}^2 \text{ m}^{-2} \text{ Hz}^{-1}$ . These figures show temporal and spatial evolution of  $n_i$  and  $T_{\perp}$  as in Figures 1a and 1b,

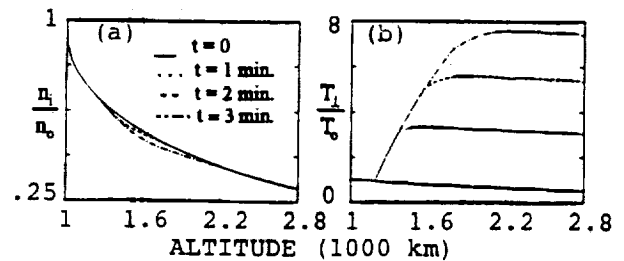


Fig. 1. (a) Evolution of density depletion in response to transverse ion heating above an altitude of 1200 km with a heating rate of  $0.014 \text{ eV}$  corresponding to a lower-hybrid wave level  $\psi = 10^{-9} \text{ V}^2 \text{ m}^{-2} \text{ Hz}^{-1}$ . (b) Evolution of  $T_{\perp}$ . Note that for the low heating rate, the relative plasma depletion  $\delta n/n < 10\%$ .

respectively. The density depletions are generally much stronger in Figure 2a than that in Figure 1a. For example at  $t=2$  min., the maximum depletion is 28% at  $h \cong 1600$  km where  $T_{\perp} = 36 T_0 \cong 18 \text{ eV}$ . At  $t=3$  min., at the same altitude, the density depletion is 36% with nearly the same value of  $T_{\perp}$ .

The heating rates considered above are within the range given by the observed power spectral density. Therefore it appears that within a few minutes after the onset of the relatively strong lower-hybrid waves, the observed levels of plasma depletions can be achieved. The results shown in Figures 1 and 2 indicate that in order to create density cavities with depletions of several tens of percent, the power spectral density near the lower-hybrid waves must exceed  $10^{-9} \text{ V}^2 \text{ m}^{-2} \text{ Hz}^{-1}$ , and the heating must last over a few minutes. It is worth pointing out that at time scales  $t > \tau_{wc}$ , the pondermotive force may continue to participate in the density depletion process because of the inhomogeneous nature of the auroral plasma. This is especially true when the wave amplitudes are sufficiently strong to yield comparable pondermotive and mirror forces.

Finally we discuss the parallel and perpendicular sizes of the density cavity. The axial size of the cavity depends on the field-aligned extent of the heating region and the duration of the heating. However, for a localized heating, the plasma expulsion produces density enhancement on top of the cavity [Singh, 1992; Singh and Chan, 1993]. On the other hand, extended heating produces a continual expulsion of the plasma into the steadily decreasing density of the polar wind with increasing altitude, without producing hardly any density

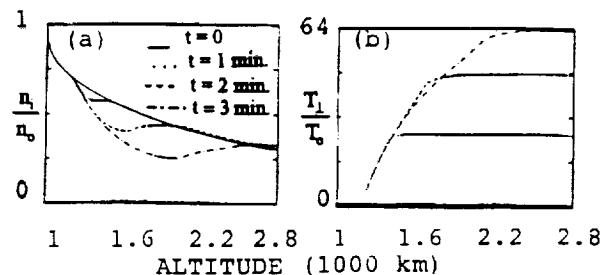


Fig. 2. (a) Same as Figures 1a, but for a heating rate of  $0.14 \text{ eV}$ . (b) Same as Figure 1b with the above heating rate. Note that the relative depletion in Figure 2a is much stronger than that in Figure 1a.

enhancement as seen from Figures 1a and 2a for  $t = 1$  and 2 minutes. Since the rocket observations do not seem to report the existence of density enhancements, it appears that the heating occurs over an extended region along the auroral field lines. The size of the cavity along the field lines depends on the heating time, as seen from Figures 1a and 2a. In view of the observed level of waves and depletions in the density cavity, the heating must be lasting at least over a few minutes, and extending over hundreds or even thousands of kilometers.

The filamentary nature of the plasma cavities having width  $\leq 100$  m probably follows from the extremely small half-cone angle ( $\theta_c$ ) of the group-velocity resonance cone of the lower-hybrid waves [Morales and Lee, 1975]. Near the lower-hybrid frequency,  $\theta_c \cong (m_e / m_i)^{1/2} \sim 5 \times 10^{-3}$  rad., which is complementary to the phase-velocity resonance cone angle. Since the electrostatic energy of the lower-hybrid wave is confined within a cone with its axis along the geomagnetic field and half cone angle  $\theta \leq \theta_c$ , the observed cavity width ( $w$ ) of  $\leq 100$  m reveals that the electrostatic lower-hybrid waves are excited by the auroral electron beams and absorbed by the plasma through the transverse heating of ions within a distance  $< w / \theta_c \cong 20$  km. The temporal and spatial features of the excitation of such waves by auroral electron beams and absorption by the thermal plasma are a challenging problem and remain to be studied.

#### Conclusion and Discussion

The main conclusions of this paper are as follows: (1) A comparison of the pondermotive and mirror forces show that the latter force on the transversely heated ions is an important factor in creating the strong plasma depletions in density cavities as observed during the lower-hybrid wave spikelet events [Vago et al, 1992]. (2) The mirror force becomes a significant force from the very early stage when ions are even slightly heated causing  $T_{\perp}$  to exceed  $T_{\parallel}$  by a fraction of an eV. (3) A model of the polar wind type of flow including transverse ion heating [Singh, 1992] shows that the heating rates given by the observed levels of lower-hybrid waves can produce density depletions consistent with the measured densities in the filamentary density cavities. The measurements indicate density depletions of a few tens of percent to be a common occurrence, but some events indicated depletions up to 80%, which were reported to occur with strong lower-hybrid waves. Model shows that for the strong depletions up to several tens of percent, the power spectral density must exceed  $10^{-8} \text{ V}^2 \text{ m}^{-2} \text{ Hz}^{-1}$ . (4) The model shows that for the observed wave levels and the depletions in the cavities, the heating events should last over a few minutes which is much longer than the time scale for the wave collapse in a homogeneous plasma. For such heating, the cavity extends to several hundred kilometers along the geomagnetic field lines.

The effectiveness of the mirror force in density depletions is contingent upon the transverse heating of ions. The lower-

hybrid waves, generated by auroral electron beams having energies of several hundred eV, are generally too fast to affect wave-particle interactions with the ions. For such an interaction the perpendicular phase velocity of the wave should be comparable to the thermal speed of the ions. In order to achieve this, the long wavelength fast waves undergo wave condensation and collapse through a modulation instability, generating short wavelength slow waves [Sotnikov et al, 1978; Shapiro et al, 1993]. During this stage, the nonlinear pondermotive force drives the modulational instability and creates plasma perturbations, which are weak and not as strong as the observed density depletions. The theory of Shapiro et al [1993] indicates that this occurs at a time scale of  $\tau_{we} \approx 0.1 \omega_{pi}^{-1} \approx 0.4$  ms for a wave amplitude of 25 mV/m. As soon as the short wavelength waves become effective in transverse heating of the ions, mirror force becomes a significant mechanism by which density depletions are created. The density perturbations created by the mirror force may further facilitate the wave trapping and enhancement.

*Acknowledgments.* This work was supported by a NASA grant NAGW-2903.

#### References

- Morales, G. J. and Y. C. Lee, Nonlinear filamentation of lower-hybrid cones, *Phys. Rev. Lett.*, **35**, 930, 1975.
- Singh, N., Plasma perturbations created by transverse ion heating events in the magnetosphere, *J. Geophys. Res.*, **97**, 4235, 1992.
- Singh, N. and C. B. Chan, Numerical simulation of plasma processes driven by transverse ion heating, *J. Geophys. Res.*, **98**, 11, 677, 1993.
- Singh, N. and R. W. Schunk, Energization of ions in the auroral plasma by broadband waves: Generation of ion conics, *J. Geophys. Res.*, **89**, 5538, 1984.
- Sotnikov, V. I., V. D. Shapiro, and V. I. Shevchenko, Macroscopic consequences of collapse of the lower-hybrid resonance, *Sov. J. Plasma Phys., Eng. Transl.*, **4**, 252, 1978.
- Vago, J. L., P. M. Kintner, S. W. Chesney, R. L. Arnoldy, K. A. Lynch, T. E. Moore and C. J. Pollack, Transverse ion acceleration by localized lower-hybrid waves in the topside auroral ionosphere, *J. Geophys. Res.*, **97**, 16, 935, 1992.
- Shapiro, V. D., V. I. Shevchenko, G. I. Solov'ev, V. P. Kalinin, R. Gingham, R. Z. Sagdeev, Ashaur-Abdalla, J. Dawson and J. J. Su, Wave collapse at the lower-hybrid resonance, *Phys. Fluids*, **B5**, 3148, 1993.

Nagendra Singh, Department of Electrical and Computer Engineering, The University of Alabama in Huntsville, Huntsville, AL 35899.

Received: September 27, 1993

Revised: November 1, 1993

Accepted: November 23, 1993

# Numerical Simulation of Plasma Processes Driven by Transverse Ion Heating

NAGENDRA SINGH AND C. B. CHAN

*Department of Electrical and Computer Engineering, University of Alabama, Huntsville*

Numerical simulation is performed to study the plasma processes driven by transverse ion heating in a diverging flux tube. It is found that the heating drives a host of plasma processes, in addition to the well-known phenomenon of ion conics. The additional processes include formation of a density cavity topped by a density enhancement, formation of a reverse and forward shock pair with a "double-sawtooth" structure in the flow velocity. The downward electric field near the reverse shock generates a doublestreaming situation consisting of two upflowing ion populations with different average flow velocities. A double streaming also occurs above the forward shock, where the ions energized by the heating are overtaking the relatively slow ions in the ambient polar wind. The energized ions appear as "elevated" ion conics with a low-energy cutoff depending on the distance from the heating region. The parallel electric fields generated by the transverse ion heating have the following noteworthy features; the electric field near the forward shock is essentially unipolar, and it points upward, and for the heating localized in both space and time, the field has the features of a weak double layer. The electric field in the reverse shock region is modulated by the ion-ion instability driven by the multistreaming ions. The oscillating fields in this region have the possibility of heating electrons. The results from the simulations are compared with results from a previous study based on a hydrodynamic model. Effects of spatial resolutions afforded by simulations on the evolution of the plasma are discussed, demonstrating how a crude resolution can miss out plasma instabilities, affecting the plasma flow.

## 1. INTRODUCTION

Transversely heated ions are a common feature of the Earth's magnetosphere. Since the early observations of such ions during the late seventies [e.g., *Whalen et al.*, 1978; *Klumpar*, 1979], a great deal of work has gone into understanding the generation and transport of such ions [e.g., *Chang*, 1986; *Klumpar*, 1986]. However, most treatments on the transport employ the test particle approach, in which a perpendicularly heated ion is transported under the action of the upward mirror force proportional to the gradients in the magnetic field. Only recently, time-dependent models have been employed to study the generation and transport processes and their effects on the ambient plasma [*Ganguli and Palmadesso*, 1987; *Brown et al.*, 1991; *Singh*, 1992]. The aspect of the plasma perturbations created by the transverse ion heating was emphasized by *Singh* [1992]. Among the noteworthy features of the plasma perturbations are the formation of density depletion and enhancement, and generation of parallel electric fields. For impulsive heating, an interesting feature of the parallel field is that it occurs in the form of a nearly unipolar upward pointing electric field pulse, which moves upward with a velocity of several tens of kilometers per second. However, a large-scale model dealing with distances of thousands of kilometers is limited in its temporal and spatial resolutions. On the other hand, electric fields seen in the auroral plasma [*Temerin et al.*, 1982] have spatial size of a few meters and corresponding time scale of about a few milliseconds. Therefore, in the previous work of *Singh* [1992], it was not clear at all how such an electric field pulse can be compared with weak double layers.

The purpose of this paper is to study the perturbations

created by the transverse ion heating, using a small-scale particle-in-cell code having the capability of resolving distances of a few Debye lengths and time of a few milliseconds. The particle simulation reveals the same basic feature of the plasma perturbations generated by the transverse ion heating as seen from the large-scale hydrodynamic study, namely, the formation of a density cavity topped by a density enhancement, and eventually, the evolution of the density perturbation into a reverse-forward shocks pair. The unipolar upward pointing electric field occurs near the forward shock. The maximum electric field in the pulse is a few millivolts per meter, and its spatial dimension is a few tens of meters. These features of the pulse, including its upward velocity of about 50 km/s, have striking resemblance with the weak double layer seen from satellite [*Temerin et al.*, 1982; *Boström et al.*, 1988].

Kinetic simulations show additional noteworthy features involving multistreaming of ions. Above the perturbations in the density, ions with relatively large energies stream upward, setting up an ion conic type of flow on top of the ambient polar wind. In the midst of the density depletion and the enhancement, two streams of up flowing ions appear, which eventually couple together through ion-ion instability. It is interesting to point out that if the grid size in the simulation is increased beyond a certain limit, the ion-ion instabilities are not seen. This implies an important limitation of large-scale models, in which the usage of large grid size eliminates the possibility of coupling the ion streams. Furthermore, the large grid size and the corresponding large time steps eliminate the process of steepening of a compressive density perturbation forming a shock, like the forward shock near the density enhancement.

The fast ions above the forward shock appear like "elevated" ion conics with a low cutoff energy, which increases with increasing distance from the heating region. Furthermore, the density of such conics decreases monotonically with the distance. This suggests that ion conics can be found far from the regions of strong density perturbations in the plasma, created by the heating process.

Copyright 1993 by the American Geophysical Union.

Paper number 92JA02789.  
0148-0227/93/92JA-02789\$05.00

The rest of the paper is organized as follows. The simulation technique is described in section 2. Numerical results on the plasma perturbations are described in section 3. The paper is concluded in section 4.

## 2. SIMULATION MODEL

We use a particle-in-cell code to solve for the dynamics of ions flowing along a diverging flux tube (Figure 1). The electrons are assumed to obey the Boltzmann distribution, which in conjunction with the quasineutrality condition yields the electric field parallel to the magnetic field. As mentioned in the introduction, the flux tube simulated is artificial in the sense that magnetic field is reduced by a factor of 2 over a distance of about  $s_{max} = 7.5$  km. This is done to hasten the transport of the transversely heated ions by the mirror force. The ion heating occurs over a limited region of space (Figure 1). Ions in this region are given a random impulse  $\delta w_{\perp}$  in the perpendicular direction according to a Maxwellian probability density function given by [Brown et al., 1991; Puri, 1966]

$$P(\delta w_{\perp}) = \frac{1}{\sqrt{\pi}\sigma} e^{-\delta w_{\perp}^2/\sigma^2}. \quad (1)$$

The energy of the ions is given by

$$w_{\perp f} = w_{\perp i} + \delta w_{\perp} + 2\sqrt{w_{\perp i}|\delta w_{\perp}|\cos\phi} \quad (2)$$

where  $w_{\perp i}$  and  $w_{\perp f}$  are the perpendicular energies of the ions at the beginning and end of a time step, and  $\phi$  is an angle between 0 and  $2\pi$  randomly chosen from a uniform probability density function. The heating rate is related to  $\sigma$  according to  $\sigma = 1.14\Delta t(\partial w_{\perp}/\partial t)$ , where  $w_{\perp} = 1/2mV_{\perp}^2$ ,  $m$  is the ion mass and  $V_{\perp}$  is the perpendicular velocity.

The ion motion is advanced by solving the equation of motion

$$m \frac{d^2 s}{dt^2} = qE_{\parallel} - \mu \frac{\partial B}{\partial s} \quad (3)$$

where  $m$  and  $q$  are the mass and charge of an ion,  $E_{\parallel}$  is the electric field,  $\mu$  is the magnetic moment of the ion, and  $\partial B/\partial s$  is the gradient in the magnetic field.

The parallel electric field,  $E_{\parallel}$ , is calculated by assuming that the plasma remains quasineutral, i.e.,  $n_e \approx n_i$ , where  $n_e$  and  $n_i$  are the electron and ion densities, respectively. Furthermore, electrons are assumed to be a massless isothermal fluid. The electron momentum equation gives

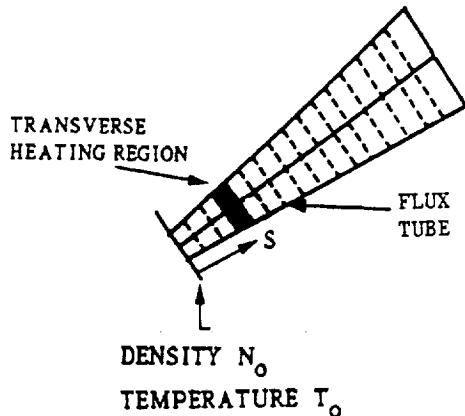


Fig. 1. Geometry of the simulated flux tube.  $N_0(20 \text{ cm}^{-3})$  and  $T_0(0.3 \text{ eV})$  are the boundary values of plasma density and ion temperature.

$$E_{\parallel} = -\frac{kT_e}{e} \frac{1}{n_e} \frac{\partial n_e}{\partial s} \quad (4)$$

where  $k$  is the Boltzmann constant and  $T_e$  is the electron temperature.

As we will see later, the scale lengths in the plasma perturbations studied here are several tens of meters while the plasma Debye length is a few meters. Therefore the space charge effects are ignorable and quasineutrality is a good approximation. The assumption of electrons being massless eliminates the effects of velocity gradients in the flow. Since in the present calculations we assume that there is no field-aligned current and  $n_e \approx n_i$ , it is implied that  $V_e = V_i$ , where  $V_e$  and  $V_i$  stand for electron and ion flow velocities, respectively. In the calculations presented here, we assume  $T_e = 1 \text{ eV}$ , for which electron thermal velocity,  $V_{te} \approx 400 \text{ km/s}$ . In the perturbations discussed in this paper, the flow velocities  $V_e$  and  $V_i \leq 15 V_{ti}$ , where  $V_{ti}$  is the ion thermal velocity, which is about  $5.5 \text{ km/s}$ . Therefore we find that  $V_e^2 \approx V_i^2 \ll V_{te}^2$ . This ensures that the assumption of electrons being massless is justified. Furthermore, it also justifies the assumption of electrons being isothermal.

## 3. NUMERICAL RESULTS

### 3.1. Summary of Results From the Fluid Model

The origin of this paper lies in a previous paper [Singh, 1992], in which plasma perturbations created by transverse ion heating were studied, using a large-scale model based on fluid equations for the plasma. Since our goal in this paper is to examine how the results from a kinetic treatment of ions compare and contrast with the results from the fluid treatment, it is useful to briefly review the latter results. Figures 2a to 2h show the basic nature of the perturbations in density, flow velocity, parallel temperature, perpendicular temperature, and the parallel electric field when the heating occurs over 5s over a heating region of 210-km length at an altitude of 5500 km. The heating rate is 240 eV/s and electron temperature is assumed to be 10 eV. Figures 2a to 2h show the evolution of the perturbation up to  $t = t_1 = 2 \text{ min}$ . Note that  $t_n = \pi \times 30 \text{ s}$ . We find that at an early time ( $t \leq t_1$ ) the basic feature of the perturbation is the formation of a plasma cavity topped by a density enhancement (Figure 2a). At later times, the density perturbation evolves into a reverse-forward shock pair, as indicated by "R" and "F". The leading edge of the perturbation is the forward shock (F) and the trailing edge of the density enhancement is the reverse shock (R). The entire perturbation is seen moving upward. However, the trailing edge of the perturbation moves much slower than the leading edge (F), resulting in the creation of an extended cavity which expands upward. Figure 2b shows that the flow velocity is perturbed over the entire region of the density perturbation and it has the feature of a double sawtooth; the tooth near the forward shock is sharp, while near the reverse shock it is relatively shallow. When the heating continues for a longer time, the reverse shock also evolves into sharp jumps [Singh, 1992].

The temperature profile for  $T_{\parallel}$  shows a cooling in the plasma cavity and an increase in the density enhancement between the reverse and forward shocks. The transverse heating yields a maximum perpendicular temperature of 100 eV at  $t = t_1$  and the maximum temperature adiabatically decreases later on. The enhancement in  $T_{\perp}$  is limited to altitudes below the forward shock. Later we show how this



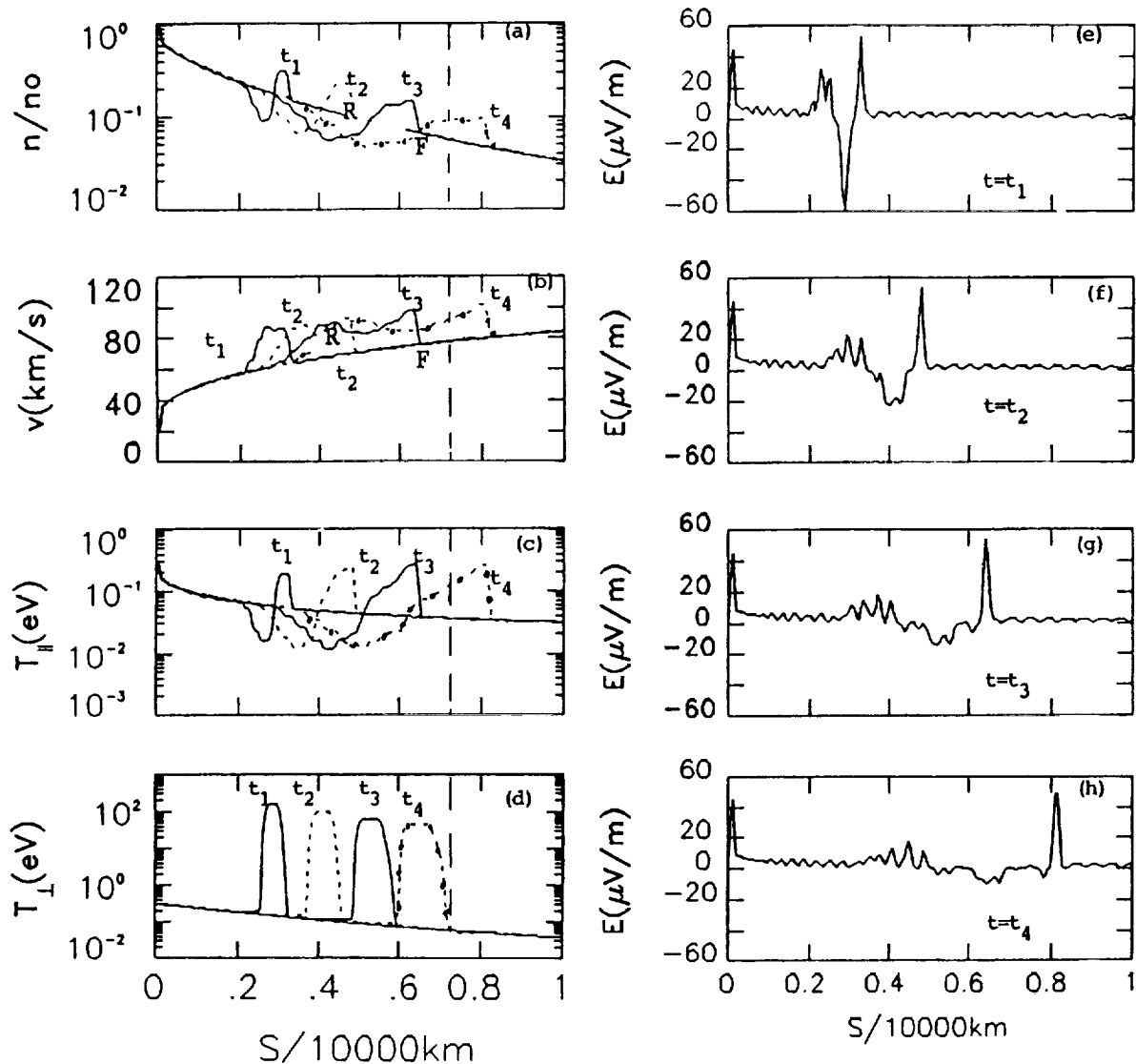


Fig. 2. Plasma perturbations in response to an impulsive heating both in time and space ( $\Delta t_h = 5$  s,  $\Delta s_h = 60$  km). Electron temperature  $T_e = 10$  eV. (a) to (d) The evolutions of  $n(s)$ ,  $v(s)$ ,  $T_{||}(s)$  and  $T_{\perp}(s)$ , respectively. (e) to (h) The evolution of the electric fields distribution.

feature is appreciably modified when the ions are treated kinetically.

The electric field perturbations for the transverse heating are shown in Figures 2e to 2h. The most noteworthy feature of the electric field distribution shown in this figure is its evolution to predominantly unipolar upward pointing electric field near the leading edge of the density bump when  $t \geq t_2 \approx 1$  min. This dominant electric field pulse propagates upward with a velocity of about 60 km/s, which is about twice the  $H^+$  ion acoustic speed with 10-eV electrons. Such upward propagating electric field pulses appear quite similar to the predominantly unipolar electric fields observed in the auroral plasma [Temerin *et al.*, 1982]. However, the observed fields are generally interpreted as ion acoustic double layers which have scale length of a few tens of Debye lengths ( $\sim 100$  m). In contrast, in the hydrodynamic calculations we have a spatial resolution of 60 km and temporal resolution of 1s, which are, respectively, the intergrid spacing and the time step used in our calculations. In the follow-

ing discussion, we present results from a kinetic treatment of ions with spatial and temporal resolutions capable of resolving ion dynamics at a time scale of ion-plasma period.

### 3.2. Results From a Small-Scale Kinetic Model

We first ran the simulation without any heating until a polar wind type of flow is set up in the artificial flux tube. For the parameters chosen here, this takes about  $1200 \omega_{pi0}^{-1}$ , where  $\omega_{pi0}$  is the ion plasma frequency at  $s = 0$ , where normalized density is unity. When the flow is established, the heating is switched on over the spatial region  $50 \leq s/\lambda_{di} \leq 250$ . The heating rate  $\partial W_{\perp}/\partial t$  is about  $\omega_{pi0} k T_0$ , where  $k$  is the Boltzmann constant and  $T_0$  is the ion temperature at the boundary  $s = 0$ . The flux tube length is  $S_{max} = 7500 \lambda_{di}$ . For the parameters chosen here the plasma density at the bottom of the flux tube is  $20 \text{ cm}^{-3}$  and temperature  $T_0 = 0.3$  eV, giving ion Debye length  $\lambda_{di} \approx 1$  m,  $S_{max} = 7.5$  km and heating rate ( $\partial W_{\perp}/\partial t$ ) is  $1800 \text{ eV/s}$ . The heating is kept on over a time period of  $\Delta t_h = 40 \omega_{pi0}^{-1} \approx 5$  ms.

### 3.3. Perturbation in Phase Space

The evolution of the heated ions is shown in Figures 3a and 3b which give the temporal evolution of phase-space in  $S - V_{\parallel}$  and  $S - V_{\perp}$  planes, respectively. At  $\bar{t} = 1400$ , where  $\bar{t} = t\omega_{pi0}$ , heated ions are still relatively localized near the heating region. At later times they flow upward under the action of the mirror force leading to an increase in parallel velocity (energy) at the expense of the perpendicular velocity (energy). As the ions flow upward, the phase-space plots show that double streaming develops both near the top and bottom of the perturbation. The two streams at the top consist of transversely heated ions, which have gained considerable parallel energies under the action of the mirror force, and the ambient polar wind ions. The relative parallel velocity between these two ion populations is sufficiently high and therefore they do not show any sign of ion-ion interaction causing instability [Gresillon and Doveil, 1975].

In the bottom most part of the perturbation ions appear to be primarily accelerated in their parallel velocities, but above a certain height depending on time, another stream appears. The latter stream is relatively slower. In the regions where these streams overlap, there are vortices in the  $S - V_{\parallel}$  plots. These vortices are the consequence of ion-ion instability, which we shall discuss later on. By the time  $\bar{t} \approx 2200$ , the major part of the perturbation in terms of transversely heated ions has almost exited from the top of the

flux tube, but there are still perturbations persisting in  $V_{\perp}$  extending to much lower heights.

The distribution function of the ions in the perturbation region ( $3750 \leq S/\lambda_{di} \leq 7500$ ) is shown for  $\bar{t} = 1800$  in Figure 4a, which gives the scatter plots of ions in  $V_{\perp} - V_{\parallel}$  plane. Transverse acceleration of ions and associated parallel acceleration due to the mirror force is clearly seen. However, we also find some ions gaining only a parallel energy corresponding to the increase in parallel velocity up to  $V_{\parallel} \approx 15V_{ti}$ . This parallel acceleration is the consequence of the random nature of the ion heating; ions gain perpendicular energies at some stage of the heating and then lose a part of it at a later stage, after they have moved upward, and converted a part of the earlier gained energy into their

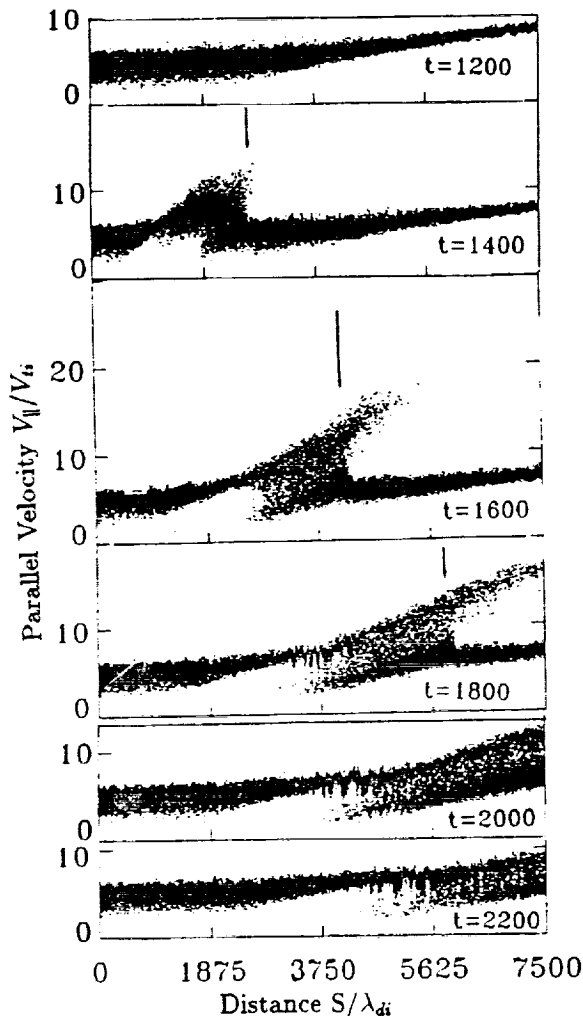


Fig. 3a. Phase-space plots in  $S - V_{\parallel}$  plane.

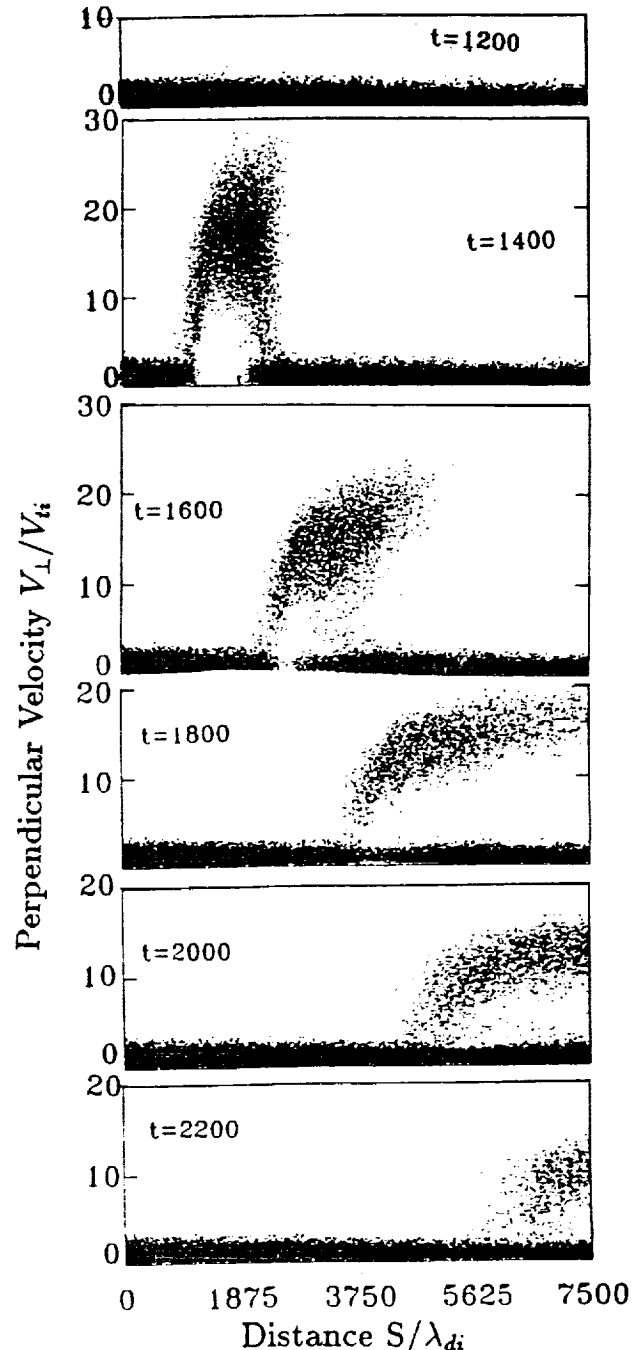


Fig. 3b. Phase-space plots in  $S - V_{\perp}$  plane.

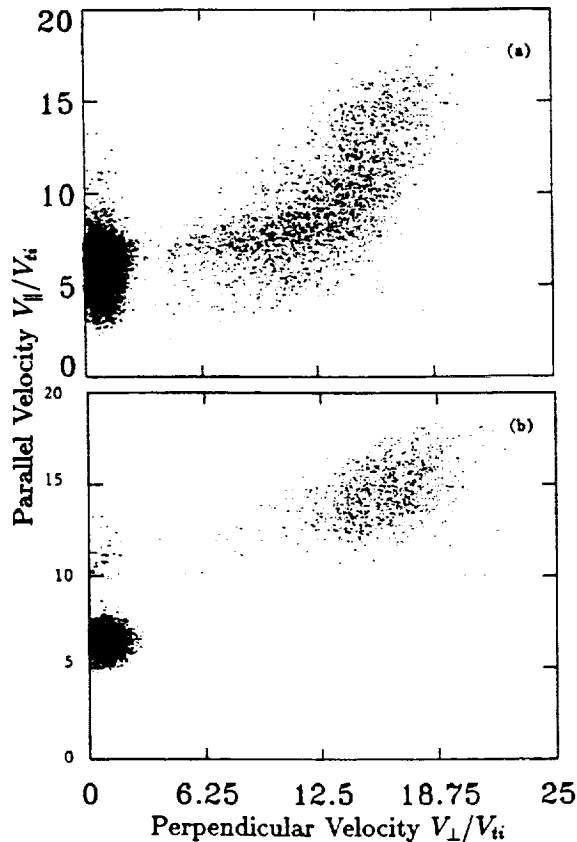


Fig. 4. Distribution of heated ions in  $V_{\perp} - V_{\parallel}$  plane for (a) entire perturbation ( $3700 \leq s/\lambda_{di} \leq 7500$ ) and (b) above the forking point ( $s > 6000\lambda_{di}$ ) at  $\tilde{t} = 1800$ .

parallel velocity component. However, the important feature of the random heating is the production of ion conics elevated in parallel energy. The elevation in parallel energy is more clearly seen if only the ions above the strong perturbation in the density, where double streaming occurs, are examined. This is shown in Figure 4b for ions with  $S > 6000\lambda_d$  at  $\tilde{t} = 1800$ .

#### 3.4. Perturbation in Average Flow Properties

We now compare the basic features of the plasma perturbations produced by the heating in the hydrodynamic (Figures 2a to 2h) and kinetic models. For the latter model, the evolution of the perturbations in the bulk plasma parameters such as density, flow velocity, and effective parallel and perpendicular temperatures are shown in Figures 5a to 5d. It is important to point out that the comparison is not quantitative, only the basic features of the perturbations are compared here. As expected the localized heating creates a density cavity topped by a density enhancement. The entire perturbation rides on top of an upward expanding polar wind into a plasma cavity created by the heating. Unlike in the hydrodynamic model (see Figure 2a), the leading portion of the density enhancement has a perturbation extending to relatively large distances. The extended perturbation is the consequence of the fast ions running ahead of the major perturbation in the density (see Figure 3). However, like in the hydrodynamic model [Singh, 1992], there is a sharp gradient near the leading edge of the density enhancement and it occurs where the  $S - V_{\parallel}$  phase-space plot forks into two

distinct branches consisting of the ambient polar wind and the transversely accelerated ions as indicated by downward arrows in Figure 3a. Below the fork, the hydrodynamic predictions are expected to be true and above it, double streams occur with large relative velocities, and the hydrodynamic model fails. The sharp gradient in the density profile is the forward shock found from a hydrodynamic model [Singh, 1992]. The shock separates the fast streaming ions above it from the mixed, and relatively warm just below it.

The velocity profiles in Figure 5b show that at  $\tilde{t} = 1400$ , the perturbation is beginning to develop a double-sawtooth structure and it is fully developed at  $\tilde{t} = 1600$ . The lower sawtooth in the perturbation occurs near the trailing edge of the density enhancements, where downward electric fields occur and retard the upward flow of transversely heated ions. This retardation of ions produces the doublestream (Figure 3a) feature in the reverse shock region. The hydrodynamic model fails to handle such a double-streaming. The top sawtooth occurs near the leading edge of the density enhancements, the forward shock. However, due to the fast ions running ahead of the forward shock, the slope of the leading tooth is considerably reduced. For later times shown in Figure 5b, the upper sawtooth has exited from the top and only the lower sawtooth can be seen.

It is worth noting that above the forking point in  $S - V_{\parallel}$  space (Figure 3a), where double streams occur, the average flow velocity does not give the true velocity of the transversely heated ions because the relatively dense cold stream (polar wind) weighs down the flow velocity. As mentioned earlier, this region is not treated properly by a hydrodynamic model.

In Figure 5c, we show the evolution of the effective parallel temperature calculated from the equation

$$T_{eff}(l\Delta s) = \sum_{j=1}^N m_i (V_j - V)^2 / N \quad (5)$$

where  $N$  is the number of particles in a cell of length  $\Delta s = 75\lambda_{di}$ , and  $l\Delta s$  is the distance from  $s = 0$  with  $l$  as an integer.

The parallel temperature profiles show a cooling of ions in the lowest part of the perturbation. Cooling occurs as the polar wind expands into the plasma cavity created by the transverse ion heating. Such a cooling is also predicted by the hydrodynamic model (Figure 2c). However, the effective temperature is seen to be elevated considerably beyond the forking point in the phase-space plots in  $S - V_{\parallel}$  plane (Figure 3a). This is simply because above the forking point there are double streams and the concept of a single temperature for the entire ion population is not valid.

The evolution of the effective perpendicular temperature is shown in Figure 5d. In this case also, it is worth mentioning that above the forking point in  $S - V_{\parallel}$  phase-space, there are two streams and the effective temperature does not give the true picture of the heated ions because the relatively dense cold ion stream (polar wind) weighs down the temperature significantly. It is important to point out that the heated ions above the forking point in the  $S - V_{\parallel}$  plots (Figure 3a) are completely lost in a hydrodynamic model, and these are the ions which appear as ion conics (Figure 4a and 4b). There are heated ions even below the forking point, but they represent an ion population having undergone a bulk heating, as a consequence of the merger of the polar wind and transversely heated ions. The hydrodynamic model can properly handle this portion of the perturbation.

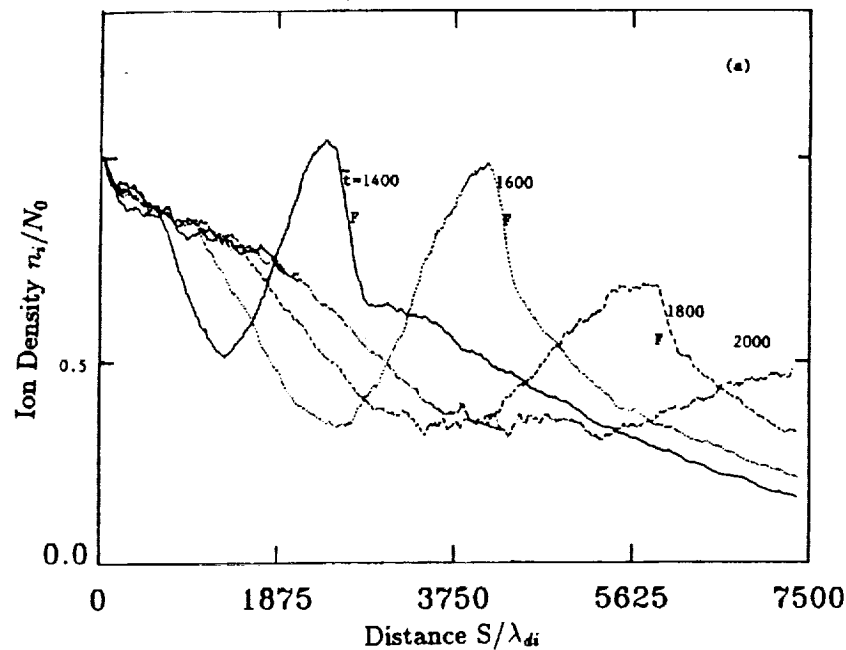


Fig. 5a. Perturbation in plasma velocity.

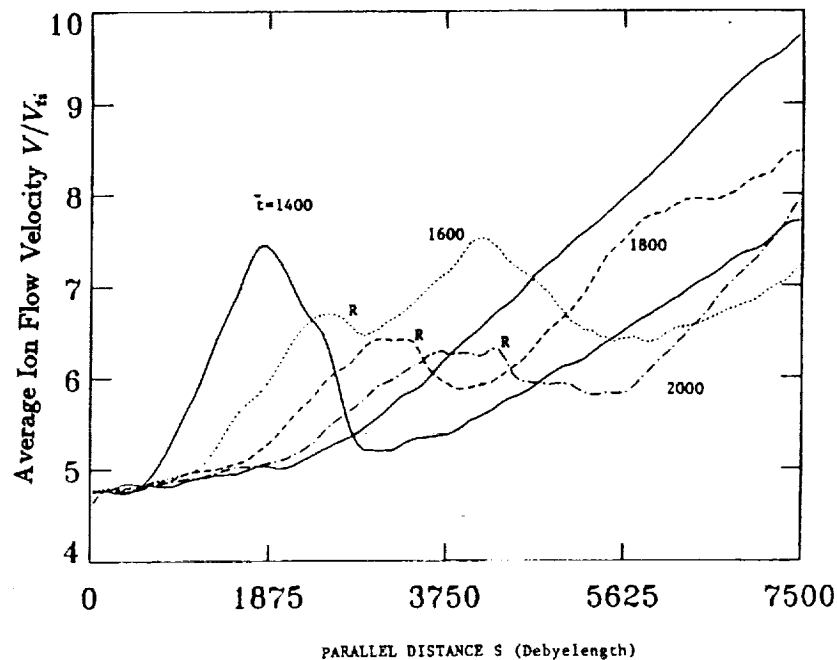


Fig. 5b. Perturbation in flow velocity.

### 3.5. Parallel Electric Field Generation

Figure 6 shows the evolution of the parallel electric field generated by the transverse ion heating. The plot at  $\bar{t} = 1200$  shows essentially the noise in the simulation system just before the heating. At  $\bar{t} = 1400$ , we notice the development of a triplet in the electric field perturbation, consisting of upward (positive) fields in its bottom most part, downward (negative) fields in the middle, and a relatively localized solitary pulse with upward fields near its top. As the composite perturbation evolves, the solitary electric field pulse moves upward with a nearly constant speed; the propagation of

the pulse is indicated by the slant line giving the trajectory of the peak of the pulse in  $s$ - $t$  plane. The trajectory is obtained by projecting the peak point on the horizontal axis and joining the projection points in the panels for  $\bar{t} = 1600, 1800$  and  $2000$  in Figure 6. The slope of this line gives the propagation speed to be about  $8.4V_{th}$ , which is about  $46 \text{ km/s}$  for the parameters chosen for the run. The pulse width of the electric field is about  $200 \text{ m}$ . The maximum field strength is about  $6 \times 10^{-3} E_0 \approx 2 \text{ mV}$ . However, it is worth mentioning that the field strength depends on the electron temperature as given by equation (4). For higher

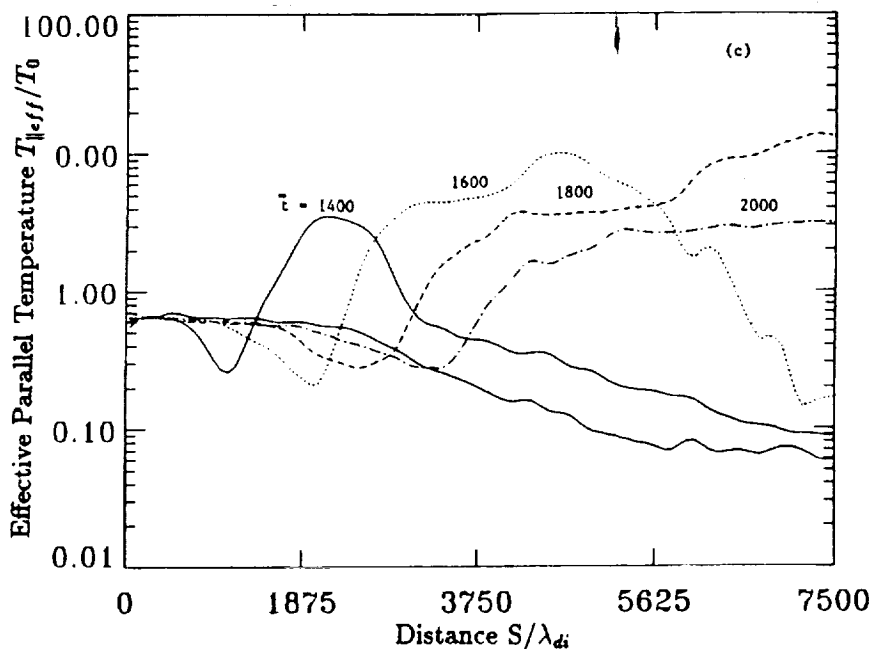


Fig. 5c. Perturbation in parallel temperature.

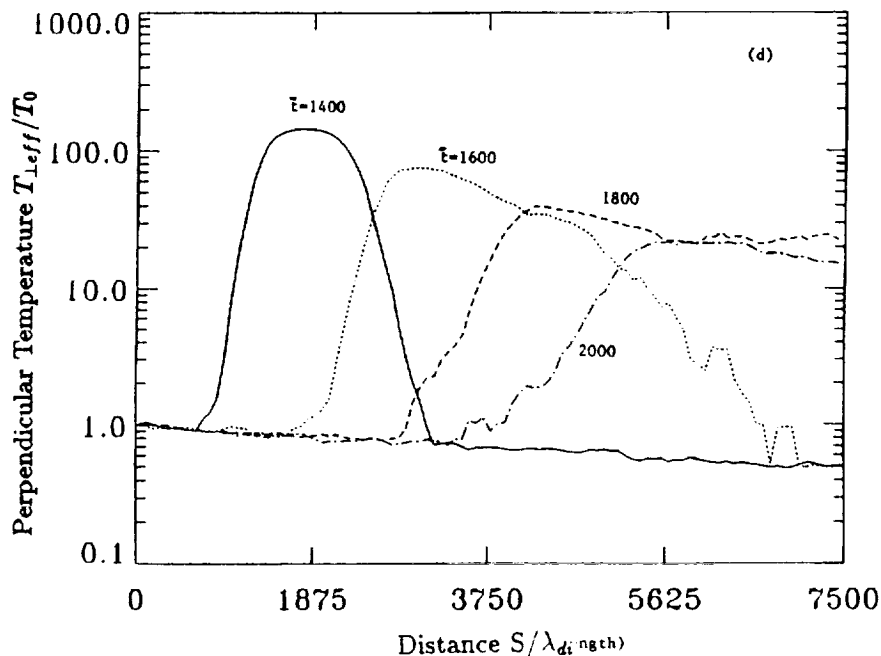


Fig. 5d. Perturbation in perpendicular temperature.

electron temperatures, a higher field strength is expected. For example, if  $T_e$  was chosen to be 10 eV, fields up to 20 mV/m are expected, and for  $T_e = 100$  eV, the fields scale to be as high as 200 mV/m. Even the shock processes may enhance  $T_e$  and hence the electric field. [Forslund and Shonk, 1970]. The electron temperature enhancement occurs when the electrons are trapped in the potential well created by the density enhancement. However, in the present calculations we have assumed electrons to remain isothermal and hence such effects are not included.

Figure 6 shows that, in the wake region of the solitary electric field pulse, oscillating fields develop. Such fields are

clearly seen for  $\bar{i} \geq 1600$  and they are well developed at  $\bar{i} \geq 2000$ . The amplitude of the wave is seen to increase to  $8 \times 10^{-3} E_0 \approx 2.5$  mV/m. The oscillating fields are associated with vortices in  $S - V_{||}$  phase space (Figure 3a). The vortices can be barely seen from Figure 3. Therefore, we have replotted them on an expanded scale in Figure 7 for  $\bar{i} = 2200$ ; the vortex size ranges between 100 to 250  $\lambda_{di}$ , which corresponds to the range in the wavelength of the spatial oscillations in the parallel fields. The vortices occur over  $3750 \leq s/\lambda_{di} < 5625$ , which is the spatial region in which the oscillating fields occur at this time (see Figure 6e).

The ion-ion instability occurs when the relative velocity

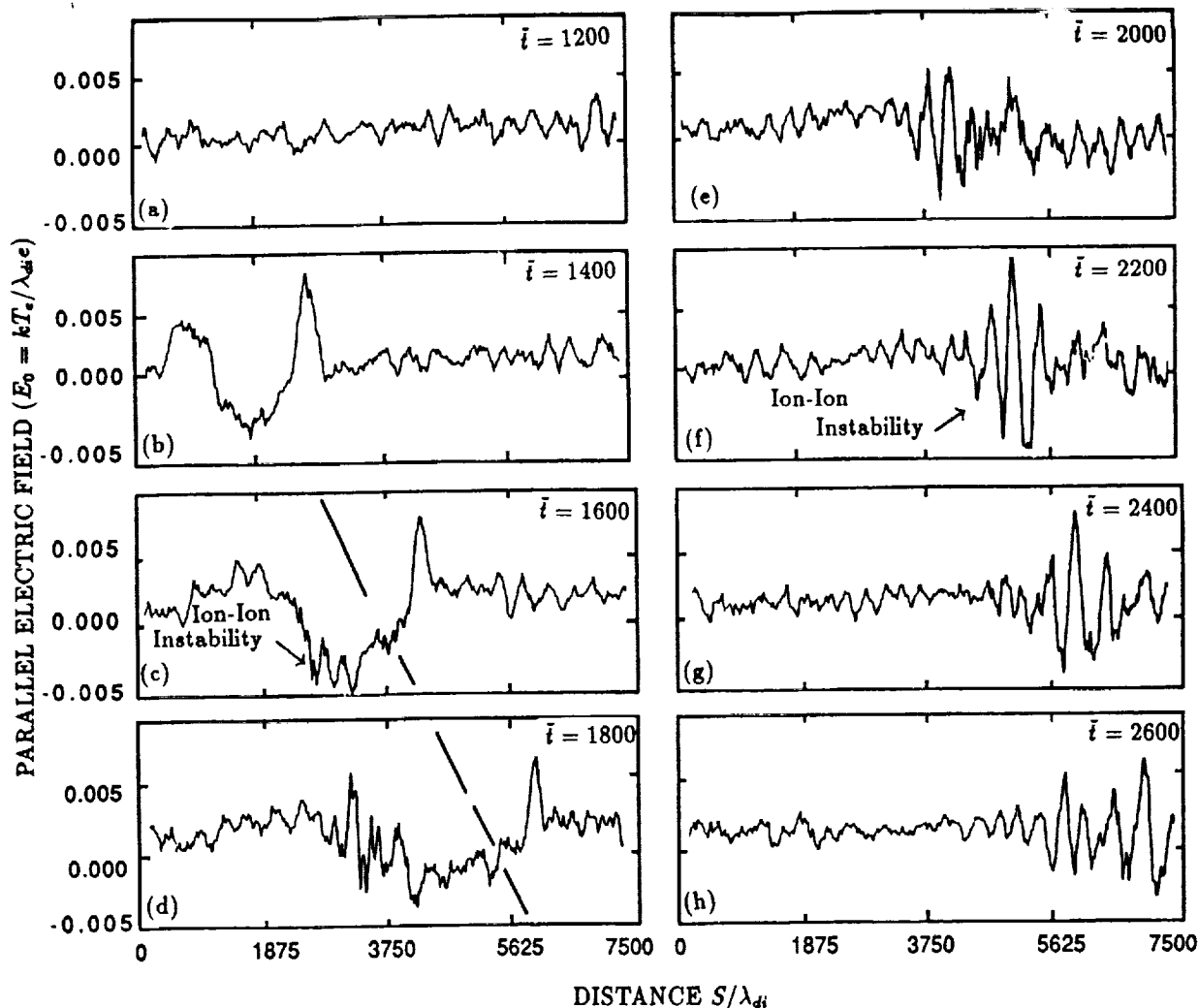


Fig. 6. Evolution of the parallel electric fields; different panels show electric field profiles at the times indicated in the panels.

( $V_{rel}$ ) between the streams is limited to  $V_{rel} \leq 2C_s$  [e.g., *Gresillon and Doveil, 1975; Singh, 1978*], where  $C_s$  is the ion-acoustic speed. In our calculation,  $T_e = 3.3T_0$ , for which  $C_s \approx 2V_{ii}$ , where  $V_{ii}$  is the ion thermal velocity given by  $(kT_0/m)^{1/2}$ . Thus the coupling is expected to occur when  $V_{rel} \leq 4V_{ii}$ . The space-phase plots (Figure 3a) show that for the double streaming in the reverse shock region, this velocity condition is well satisfied. On the other hand, for the double streaming above the forward shock, the two streams are generally too fast to drive the ion-ion interaction. However, for such fast streams ion-electron interaction may lead to instabilities, which occur when the negative energy (slow) mode of an ion beam is damped by the Landau damping caused by the thermal electron population [*Singh, 1978*]. In the present model, electrons are assumed to obey the Boltzmann Law, so this kinetic instability is suppressed from the model.

### 3.6. Numerics Versus Physics

Plasma problems in space involve a wide variety of scale lengths, ranging from plasma Debye length to the geophysical distances. This makes it impossible to develop self-consistent models including both small- and large-scale pro-

cesses. Recently, large-scale semikinetic models have been developed to study the polar wind [*Wilson et al. 1990; Brown et al., 1991; Ho et al., 1992*] and the plasmaspheric refilling [*Lin et al., 1992; Wilson et al., 1992*]. These models employ a particle code in which the number of particles is limited to about  $10^5$ , filling a flux tube of length up to several earth radii. Thus the models have, on the average, about 1 particle per kilometer. In these models, electric fields are calculated from the ion density, which is obtained by the number of particles in numerical cells and their volumes. In order to have reasonable statistics, the cell size is typically several tens of kilometers. Due to these reasons, the large-scale kinetic models suppress the microprocesses, even though the codes treat ions kinetically.

In order to demonstrate the above points on how the numerics suppress the physical processes, we repeated the calculations presented earlier with different grid sizes for calculating the electric fields. The evolution of  $S - V_{ii}$  phase space for different grid sizes is shown in Figures 8a to 8f;  $\Delta s = 5\lambda_d$  for Figures 8a and 8b;  $\Delta s = 20\lambda_d$  for Figures 8c and 8d; and  $\Delta s = 100\lambda_d$  for Figures 8e and 8f. The left- and right-hand columns of Figure 8 show different stages of the evolution of the ion-ion instability which occur in the per-

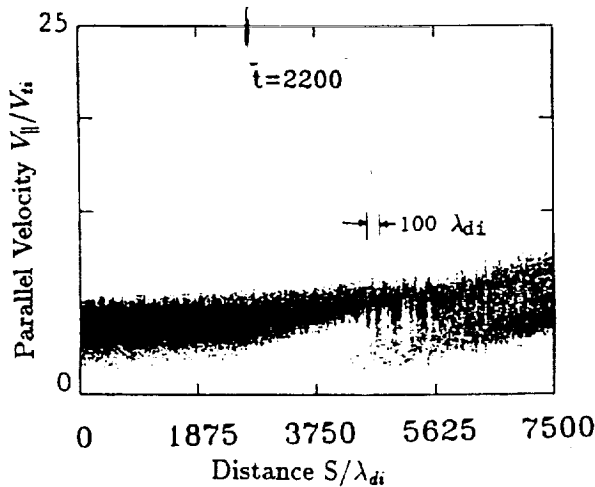


Fig. 7.  $S - V_{||}$  plot at  $\bar{t} = 2200$ , showing the vortices on an expanded scale.

turbations. For  $\Delta s = 5\lambda_d$  (Figure 8a and 8b) the instability, manifested by the vortices, is much more fine grained than that for  $\Delta s = 20\lambda_d$  (Figures 8c and 8d), for which the vortex formation is quite clear, especially at  $\bar{t} = 2200$ . When  $\Delta s$  is increased to  $100\lambda_d$  (Figures 8e and 8f), the instability does not occur at  $\bar{t} = 1800$ , and at  $\bar{t} = 2200$  the vortex structure tends to appear, but is not strong enough to fully couple the two ion streams. When  $\Delta s$  is further increased, the instability nearly disappears, even though the ion streams have nearly the same bulk properties, such as the flow velocity, density and temperature.

In order to understand the above feature of ion-ion instability and its numerical realization, we discuss here briefly its linear properties. The ion-ion instability is limited to relatively long wavelengths given by  $\lambda \geq 2\pi V_{rel}/\omega_{pi}$ , where  $V_{rel}$  and  $\omega_{pi}$  are, respectively, the local relative velocity between the streams and the ion plasma frequency. In the present situation the relative velocity is about  $4V_{ti}$ , and  $\omega_{pi} \approx 0.4\omega_{pin}$  (corresponding to a local density of 0.2 inside the cavity), giving  $\lambda \geq 80\lambda_{di}$ . However, the waves are strongly excited near the lower limit on the wave lengths [see Baker, 1973]. Therefore, when  $\Delta s = 5\lambda_d$ , the growing waves are properly described by the numerics because there are several grid spacings in a wavelength. In Figures 8a and 8b, the size of the vortices is about  $100\lambda_{di}$ . When  $\Delta s$  is increased to  $20\lambda_d$ , the relatively short wavelength waves are eliminated numerically and those left have a relatively long wavelength. In Figures 8c and 8d, the vortices are separated by about  $200\lambda_d$ . When  $\Delta s$  is increased to  $100\lambda_d$ , the instability is almost entirely eliminated by the numerics. However, Figure 8f does show a relatively weak vortex structure, as expected from the fact that the long wavelength waves, not unaffected by the large grid size, have relatively small growth rates [Baker, 1973].

The above discussion shows that in order to properly model the ion waves associated with ion streams in space, a sufficiently small resolution depending on the ion parallel energy and plasma density, is needed. For typical energies and densities in the auroral plasma at relatively high altitudes, the resolution required is  $\leq 1$  km. Therefore large-scale models even though they may be kinetic, fail to treat the microprocesses, and results from them under the conditions of counterstreaming and double streaming must be treated with caution.

#### 4. CONCLUSION AND DISCUSSION

The main aim of this paper is to study the variety of plasma processes which can be driven by localized transverse ion heating in a diverging flux tube. Although we have simulated here an artificial flux tube, the main motivation for this study is the transverse ion heating occurring in the Earth's magnetosphere, producing the well-known phenomenon of ion conics. The self-consistent generation and transport of ion conics, including the driven microprocesses, are almost impossible to model theoretically because of the range of scale lengths involved in space plasmas. Therefore, in order to develop a feel for the possible processes we have adopted an artificial diverging flux tube, in which effects of the transverse ion heating on the plasma are simulated. As described in the previous section, the results from this initial study are interesting because they show that the transverse ion heating does not just produce ion conics, it also drives a host of plasma processes, some of which are revealed here by the simulation. Among the important processes revealed are the formation and dynamics of plasma density perturbations, generation of parallel electric fields, multistreaming of ions, and ion-ion interactions generating oscillating field-aligned electric fields.

The generation of parallel electric fields by transverse ion heating is a novel concept. For heating localized to a few km, the electric field pulse near the forward shock had upward fields, it moves upward, and has the spatial and temporal features of weak double layers. Can such fields account for weak double layers observed in space [Temerin *et al.*, 1982; Block *et al.*, 1987; Boström *et al.*, 1988]? At this time this is an open question and its answer lies in a rigorous scrutiny of the theoretical results in view of the observed features of the fields in space. This has not been done here.

The above feature of the plasma perturbations driven by the transverse ion heating was previously predicted from a hydrodynamic model for the polar wind plasma flow [Singh, 1992]. However, in that study the spatial and temporal features were too coarse to predict the fine temporal and spatial features of the parallel electric fields obtained here. Figure 6 shows that the spatial size of the electric field pulse is  $\sim 100$  m; it moves with a velocity of about 50 km/s and the corresponding time scale of the pulse is 2 ms.

The double streaming of ions produced by transverse ion heating is noteworthy. The double streaming occurring in the midst of the density perturbation is the consequence of the upward acceleration of some ions by the mirror force while some ions are being retarded downward by the downward electric field in the reverse shock region. This multistreaming produces ion waves generating oscillating parallel electric fields. The role of such fields in electron heating is mentionable. However, the present simulation model does not allow it because electrons are assumed to obey the Boltzmann law.

The double streaming of ions above the forward shock is produced by the relatively slow polar wind ions being overtaken by the fast ions produced by transverse ion heating. The latter ions have the feature of "elevated" ion conics [Temerin, 1986; Horwitz, 1986; Hultqvist *et al.*, 1988]. The double streams on the top of the perturbation do not excite ion-ion instability because their relative velocity is too fast. However, the presence of relatively warm electrons may change this by increasing the ion-acoustic speed.

In the present model, electron dynamics is highly sim-

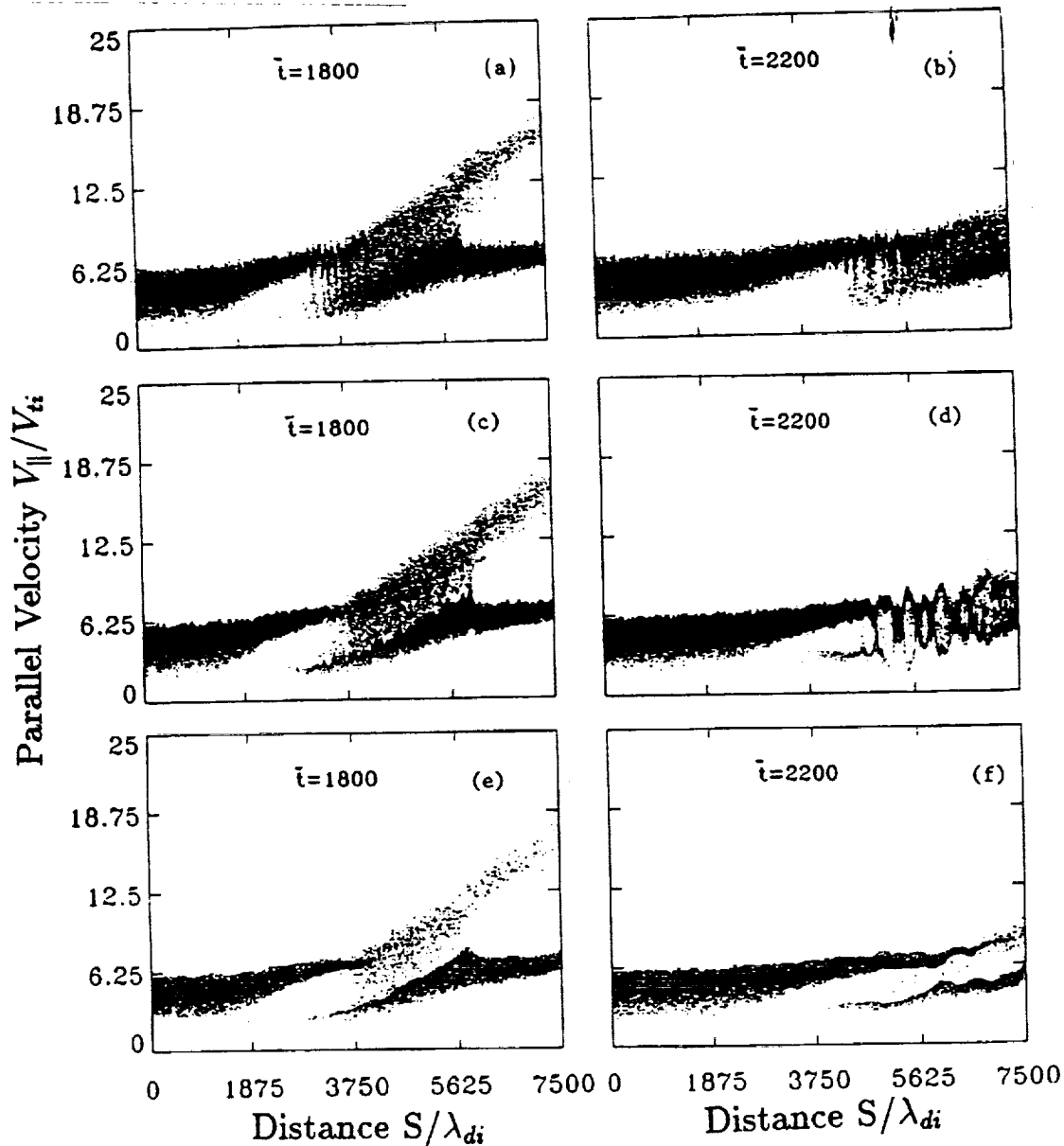


Fig. 8. Composition of  $S - V_{||}$  plots for different values of the spatial resolution: (a)  $\Delta s = 5\lambda_{di}$ , (b)  $\Delta s = 20\lambda_{di}$ , (c)  $\Delta s = 100\lambda_{di}$ .

plified through the assumption that the electrons obey the Boltzmann law. If this assumption is relaxed, electrons are likely to be energized by the parallel fields, especially by the oscillatory fields driven by ion-ion instability. One of the puzzling observations in space is the simultaneous measurement of elevated ion conics and field-aligned electrons with comparable energies [Hultqvist *et al.*, 1988]. These particle populations are observed in conjunction with electrostatic noise in the frequency range from zero to 300 Hz. The simulations presented here show how a localized heating can generate the elevated ion conics and the field-aligned electric fields which are capable of heating electrons in the parallel direction. If electron dynamics is included in the model, possibly other wave modes through ion-electron interaction can be driven. Simulations with full electron dynamics are needed to see if the puzzling observations by Hultqvist *et al.* [1988] can be explained by localized ion heating and the processes driven by it.

We have quantitatively demonstrated here how large-scale hydrodynamic and kinetic codes suppress the small-scale features of plasma flow because of their inherent coarseness. Small-scale simulations which keep the essential features of the problems in space and, at the same time, have sufficient spatial and temporal resolutions, can elucidate the important microprocesses which effectively control the properties of the plasma flow. This paper presents an initial attempt towards the goal of understanding the generation and transport of ion conics and associated plasma processes.

Results presented in this paper are based on assumptions such as (1) plasma being quasineutral, (2) electrons are a massless isothermal fluid, and (3) the simulation is one-dimensional. We already discussed that for the parameters chosen in the present simulations the assumptions 1 and 2 are justified. However, for situations involving other set of parameters, the results presented here can be only qualitatively correct. For example, if the heating produces



a large flow velocity approaching the electron thermal velocity, the assumption of electrons being isothermal is not justified. This situation requires a more rigorous treatment of the electron dynamics. We are currently investigating such situations and results will be reported later.

The assumption of one-dimensional simulation model limits the treatment of the ion-ion instability. In a multidimensional situation, ion beams with relative velocities  $V_{rel} > 2C_s$  can couple together through ion-ion instability [see Karimabadi *et al.*, 1991]. The coupling occurs through waves propagating at oblique angles with respect to the flow direction. The fast ions above the forward shock can participate in such instability processes. But the present simulation model is limited due to its dimensionality.

It is worth mentioning here that the hydrodynamic models have been used to study the transverse ion heating and their transport [Ganguli and Palmadesso, 1987; Singh, 1992]. The qualitative comparison of the results from the small-scale kinetic simulation and the large-scale hydrodynamic model shows that the latter model can not handle the phenomenon of ion conics and its transport; the temperatures and the flow velocity of the ion conics are grossly misrepresented. This is true despite the fact that the hydrodynamic models are quite sophisticated based on 16-moment approximation [Barakat and Schunk, 1982]. The major problem lies in handling the multistreaming consisting of the ion conics and the ambient plasma. Large-scale kinetic models [Wilson *et al.*, 1990; Brown *et al.*, 1991] do allow for multistreaming, but the problem lies in the coarse resolution and the consequent suppression of microprocesses which can critically affect the flow behavior. A rigorous treatment of the transport of ion conics including its interaction with the ambient plasma remains a challenge.

*Acknowledgments.* This work was supported by the Grant NAGW-2903 from NASA Headquarters to the University of Alabama in Huntsville.

The Editor thanks D. Winske and T. Onsager for their assistance in evaluating this paper.

#### REFERENCES

- Baker, D. R., Nonlinear development of the two ion beam instability, *Phys. Fluids*, **16**, 1730, 1973.
- Barakat, A. R., and R. W. Schunk, Transport equations for multi-component anisotropic space plasmas: A review, *Plasma phys.*, **24**, 389, 1982.
- Block, L. P., C. G. Fälthammar, O. A. Lindqvist, G. T. Marklund, F. S. Mozer, and A. Pedersen, Electric field measurement on Viking: First results, *Geophys. Res. Lett.*, **14**, 435, 1987.
- Boström, R., G. Gustafsson, B. Holback, G. Holgren, H. Koskinen, and P. Kintner, Characteristics of solitary waves and weak double layers in the magnetospheric plasma, *Phys. Rev. Lett.*, **61**, 82, 1988.
- Brown, D. G., G. R. Wilson, J. L. Horwitz, and D. L. Gallagher, Self-consistent production of ion conics on return current region auroral field lines: A time-dependent, semikinetic model, *Geophys. Res. Lett.*, **18**, 1841, 1991.
- Chang, T. (Ed.), *Ion Acceleration in the Magnetosphere and Ionosphere*, Geophys. Monogr. Ser., vol. 38, AGU, Washington, D. C., 1986.
- Forslund, D. W., and C. R. Shonk, Formation of electrostatic Collisionless Shocks, *Phys. Rev. Lett.*, **25**, 1699, 1970.
- Ganguli, S. B., and P. J. Palmadesso, Plasma Transport in the Auroral Current Region, *J. Geophys. Res.*, **92**, 8673, 1987.
- Gresillon, D., and F. Doveil, Normal modes in the ion-beam-plasma system, *Phys. Rev. Lett.*, **34**, 77, 1975.
- Ho, C. W., J. L. Horwitz, N. Singh, T. E. Moore, and G. R. Wilson, Effects of magnetospheric electrons on polar plasma outflow: A semi-kinetic model, *J. Geophys. Res.*, **97**, 8425, 1992.
- Horwitz, J. L. Velocity filter mechanism for ion bowl distributions (Bimodal Conics), *J. Geophys. Res.*, **91**, 4513, 1986.
- Hulqvist, B., On the acceleration of electrons and positive ions in the same direction along magnetic field lines by parallel fields, *J. Geophys. Res.*, **93**, 9777, 1988.
- Karimabadi, H., N. Omidi, and K. B. Quest, Two-Dimensional Simulations of the ion-ion acoustic instability and electrostatic shocks, *Geophys. Res. Lett.*, **18**, 1813, 1991.
- Klumpar, D. M., Transversely accelerated ions: An ionospheric source of hot magnetospheric ions, *J. Geophys. Res.*, **84**, 4229, 1979.
- Klumpar, D. M. A digest and comprehensive bibliography on transverse auroral ion acceleration in *Ion Acceleration in the Magnetosphere and Ionosphere*, Geophys. Monogr. Ser., vol. 38, edited by T. Chang, p. 389, AGU, Washington, D. C., 1986.
- Lin, J., J. L. Horwitz, G. R. Wilson, C. W. Ho, and D. G. Brown, A semikinetic model for early state plasmaspheric refilling, 2, Effects of wave-particle interactions, *J. Geophys. Res.*, **97**, 1121, 1992.
- Puri, S., Plasma heating and diffusion in stochastic fields, *Phys. Fluids*, **9**, 2043, 1966.
- Singh, N., The ion-electron instability of ion-beam-plasma systems, *Phys. Lett.*, **67A**, 372, 1978.
- Singh, N., Plasma perturbations created by transverse ion heating events in the magnetosphere, *J. Geophys. Res.*, **97**, 4235, 1992.
- Temerin, M., Evidence of a large bulk ion conic heating region, *Geophys. Res. Lett.*, **13**, 1059, 1986.
- Temerin, M., K. Cerny, W. Lottko, and F. S. Mozer, Observation of double layers and solitary waves in the auroral plasma, *Phys. Res. Lett.*, **48**, 1175, 1982.
- Whalen, B. A., W. Bernstein, and P. W. Daly, Low altitude acceleration of ionospheric ions, *Geophys. Res. Lett.*, **5**, 55, 1978.
- Wilson, G. R., C. W. Ho, J. L. Horwitz, N. Singh, and T. E. Moore, A new kinetic model for time-dependent polar plasma outflow: Initial results, *Geophys. Res. Lett.*, **17**, 263, 1990.
- Wilson, G. R., J. L. Horwitz, and J. Lin, A semi-kinetic model for early-stage plasmasphere refilling, 1, Effects of Coulomb collisions, *J. Geophys. Res.*, **97**, 1109, 1992.

C. B. Chan and N. Singh, Department of Electrical and Computer Engineering, University of Alabama, Huntsville, AL 35899.

(Received August 19, 1992;  
revised October 19, 1992;  
accepted November 23, 1992.)



# Plasma Expansion and Evolution of Density Perturbations in the Polar Wind: Comparison of Semikinetic and Transport Models

C. W. HO, J. L. HORWITZ, N. SINGH AND G. R. WILSON

*Department of Physics and Center for Space Plasma and Aeronomic Research, The University of Alabama in Huntsville*

Comparisons are made between transport and semikinetic models in a study of the time evolution of plasma density perturbations in the polar wind. The situations modeled include plasma expansion into a low-density region and time evolution of localized density enhancements and cavities. The results show that the semikinetic model generally yields smoother profiles in density, drift velocity, and ion temperature than the transport model, principally because of ion velocity dispersion. While shocks frequently develop in the results of the transport model, they do not occur in the semikinetic results. In addition, in the semikinetic results, two ion streams, or double-humped distributions, frequently develop. In the transport model results the bulk parameters, at a given time, often have a one-to-one correspondence in the locations of their local minima or maxima. This is a consequence of the coupling of the fluid equations. There is, however, no such relationship among the moments produced by the semikinetic model where the local moment maxima and minima are often shifted in altitude. In general, incorporation of enhanced heat fluxes in the transport model leads to somewhat improved agreement with the semikinetic results.

## INTRODUCTION

Numerous models have been developed in the last three decades to treat the outflow of plasma from the topside ionosphere. These models fall mainly into two categories: kinetic descriptions and hydrodynamic descriptions. Hydrodynamic models were first formulated by *Banks and Holzer* [1968]. In assuming an isothermal temperature distribution, they found that the electric field, which is determined by the electron pressure gradient, is strong enough to accelerate  $H^+$  and  $He^+$  ions to supersonic velocities. This and other related studies [*Banks and Holzer*, 1969; *Marubashi*, 1970] established the basic characteristics of the polar wind, such as the ion density versus altitude and the outflow fluxes.

Realizing that ions become collisionless and their velocity distributions highly anisotropic at sufficiently large radial distances, *Dessler and Cloutier* [1969] proposed a single-particle evaporative polar "breeze" model as an alternative to the hydrodynamic approach. They argued that ion acceleration due to the polarization electric field occurs at altitudes where the mean free path is large, and where the ions cannot be regarded as interacting directly with each other. They questioned the pressure gradient term in the hydrodynamic equations of motion and argued that it cannot be responsible for the acceleration of the light ions. This led to the famous *Banks-Holzer* and *Dessler-Cloutier* controversy which is discussed in detail by *Donahue* [1971].

Since the early theoretical models of the polar wind were established in the late 1960s and early 1970s [*Banks and Holzer*, 1968; 1969; *Holzer et al.*, 1971; *Lemaire and Scherer*, 1970; 1971], polar outflows have

been studied through the use the hydrodynamic or transport [*Schunk and Watkins*, 1981; *Mitchell and Palmadesso*, 1983; *Singh and Schunk*, 1985; 1986; *Ganguli and Palmadesso*, 1987; *Ganguli et al.*, 1987; *Gombosi and Nagy*, 1988], ion kinetic [*Horwitz and Lockwood*, 1985; *Horwitz*, 1987] and semikinetic [*Barakat and Schunk*, 1983; *Li et al.*, 1988; *Wilson et al.*, 1990; *Brown et al.*, 1991; *Ho et al.*, 1992] models.

Transport models involve the solution of a set of  $N$  moment equations solving for  $N + 1$  bulk parameters. The equation set is closed by expressing the highest moment as an assumed function of the lower order moments. The principal advantages of the transport model include its efficiency in the use of computer resources (compared to the semikinetic model) and its ability to easily include chemical and collisional processes. However, many problems require a detailed knowledge of the ion velocity distribution function beyond that which would be available from a transport model. The ability of a transport model to accurately describe the velocity distribution increases with the order of the moment equations employed, but the highest order equations can be difficult to solve [e.g., *Gombosi and Rasmussen*, 1991]. In contrast, in solving the Boltzmann equation the kinetic model solves an infinite hierarchy of moment equations since its results yield the full distribution function. This however is achieved at the expense of computer efficiency. As an approximate solution to the Boltzmann equation one can solve the gyro-averaged Boltzmann equation by a hybrid or semikinetic (kinetic ions, fluid electrons) technique.

In view of the vastly different formulations of the kinetic and hydrodynamic models applied to the same geophysical environments by different investigators over the past two decades, it is necessary to compare the two approaches in such a way so as to elucidate the differences, applicability, and limitations of the two approaches. Except for some limited work done in the

Copyright 1993 by the American Geophysical Union.

Paper number 93JA00635.  
0148-0227/93/93JA-00635\$05.00

early 70's by *Holzer et al.* [1971] and *Lemaire and Scherer* [1972], recently only *Demars and Schunk* [1992] have compared the semikinetic with the transport models for the steady state polar wind. Their results showed close agreement in the density, drift velocity, parallel and perpendicular temperatures, and parallel and perpendicular heat flows from both models. They concluded that the bi-Maxwellian based transport equations are an appropriate tool for studying space plasmas that develop non-Maxwellian features. However, good agreement between the steady state solutions from the two models does not necessarily mean that they will continue to agree when time evolving problems are considered.

The purpose of the present study is twofold. First, and foremost, is to investigate the appropriateness of using the transport model for dynamic situations, especially in the collisionless domain. This part of the study is accomplished by direct comparison of the moments produced by a transport and a semikinetic model. Of particular interest is the question of whether steep gradient persistence (i.e., shocks) are unique to the transport model. Another question involves the consequences of phase mixing [*Palmadesso et al.*, 1988] which is disallowed in the transport model because of the truncation of the moment hierarchy but is naturally included in the semikinetic model. Phase mixing can be responsible for damping thermal waves. By analyzing the degree of agreement of transport with semikinetic models, we can assess the appropriateness of using such transport models in global systems, where semikinetic modeling is currently not feasible. The second purpose of this study is to extend the work of *Singh and Schunk* [1985] on the study of the time evolution of density perturbations in the polar wind. In the present study a more sophisticated transport model and a semikinetic model are used to study the same situations considered by *Singh and Schunk*.

#### SEMIKINETIC MODEL

The semikinetic model used in this paper is the same as that developed by *Wilson et al.* [1990]. The model is based on a hybrid particle-in-cell approach which treats the ions ( $H^+$ ) as parallel-drifting gyrocenters injected, at the lower boundary, as the upgoing portions of a drifting bi-Maxwellian distribution. The electrons are treated as a massless neutralizing fluid.

We simulate the motion of  $H^+$  in a magnetic flux tube extending from 1.47 to 10  $R_B$ . Within this altitude range the plasma is taken to be collisionless. The ions at the exobase (1.47  $R_B$ ) are assumed to be bi-Maxwellian and the upgoing ions of these distributions are injected into the simulation region. The distribution function used for injecting new ions at the base of the flux tube is given by

$$f_o(v_{\parallel} \geq 0) = n_o \frac{(m/2\pi k)^{3/2}}{T_{\perp o} \sqrt{T_{\parallel o}}} \cdot \exp\left(-\frac{m(v_{\parallel} - u_o)^2}{2kT_{\parallel o}} - \frac{mv_{\perp}^2}{2kT_{\perp o}}\right) \quad (1)$$

$$f_o(v_{\parallel} < 0) = 0$$

where the subscripts  $o$  represents the various parameters of the injected ions at the base of the flux tube,  $v_{\parallel}$  and  $v_{\perp}$  are the parallel and perpendicular velocities,  $m$  is the ion mass and  $k$  is Boltzmann's constant. For this study, we use the polar wind parameters similar to *Singh and Schunk* [1985] for the injected  $H^+$  distribution functions: an upgoing drift speed ( $u_o$ ) of 20 km/s; a density ( $n_o$ ) of 500 ions/cm<sup>3</sup>; and parallel and perpendicular temperatures ( $T_{\parallel o}$ ,  $T_{\perp o}$ ) of 3560 K.

The parallel force along the magnetic field line acting on the ions is

$$F_{\parallel} = mg_{\parallel} + q_i E_{\parallel} - \mu \nabla B \quad (2)$$

where  $q_i$  is the charge of the ion,  $g_{\parallel}$  is the gravitational acceleration which varies as  $1/r^2$ ,  $\mu$  ( $= \frac{1}{2}mv_{\perp}^2/B$ ) is the ion's magnetic moment, and  $E_{\parallel}$  is the polarization electric field parallel to the magnetic field,  $B$ .  $B$  is assumed to vary as  $r^{-3}$ . The term  $-\mu \nabla B$  is the magnetic gradient or magnetic mirror force. The assumed constancy of  $\mu$  determines the perpendicular speed  $v_{\perp}$ .

By assuming that the electrons are isothermal and have zero mass, the electric field is given by the Boltzmann relation

$$E_{\parallel} = -\frac{kT_e}{n_e e} \frac{dn_e}{dr} \quad (3)$$

where  $k$  and  $e$  are the Boltzmann constant and the magnitude of the electronic charge,  $T_e$  is the electron temperature taken to be the same as the ion temperature at  $r_o$ , and  $n_e$  is the electron density which is assumed to be equal to the ion density.

#### TRANSPORT MODEL

The collisionless transport equations governing the magnetic field aligned gyrotropic motion of ions are the equations of continuity, momentum and parallel and perpendicular thermal energy given by the following:

$$\frac{\partial n}{\partial t} + \frac{\partial}{\partial s}(nv) = \frac{-nv}{A} \frac{\partial A}{\partial s} \quad (4)$$

$$\frac{\partial v}{\partial t} + \frac{\partial}{\partial s}\left(\frac{1}{2}v^2\right) = \left(\frac{q_i}{m}\right)E_{\parallel} - \left(\frac{k}{m}\right)\frac{\partial T_{\parallel}}{\partial s} - \left(\frac{k}{m}\right)T_{\parallel} \frac{1}{n} \frac{\partial n}{\partial s} - g_{\parallel}(r) - \left(\frac{k}{m}\right)(T_{\parallel} - T_{\perp}) \frac{1}{A} \frac{\partial A}{\partial s} \quad (5)$$

$$\frac{\partial T_{\parallel}}{\partial t} + \frac{\partial}{\partial s}(vT_{\parallel}) = -T_{\parallel} \frac{\partial v}{\partial s} - \frac{1}{nA} \frac{\partial}{\partial s}(q_{\parallel}A) + 2q_{\perp} \frac{1}{nA} \frac{\partial A}{\partial s} \quad (6)$$

$$\frac{\partial T_{\perp}}{\partial t} + \frac{\partial}{\partial s}(vT_{\perp}) = T_{\perp} \frac{\partial v}{\partial s} - T_{\perp} v \frac{1}{A} \frac{\partial A}{\partial s} - \frac{1}{nA} \frac{\partial}{\partial s}(q_{\perp}A) - q_{\perp} \frac{1}{nA} \frac{\partial A}{\partial s} \quad (7)$$

where  $t$  is time;  $r$  is the geocentric distance to the point along the flux tube,  $s$  is the distance along the

tube from its lower boundary,  $n$ ,  $v$ ,  $T_{\parallel}$ ,  $T_{\perp}$ ,  $q_{\parallel}$  and  $q_{\perp}$  are the number density, flow velocity, parallel and perpendicular temperatures and heat flows of the polar wind ions, respectively.  $E_{\parallel}$  is the parallel electric field (found from equation (3)),  $g_{\parallel}$  is the component of the gravitational force parallel to the magnetic field,  $m$ ,  $q_i$  and  $k$  are the ion mass, ion charge and Boltzmann constant, respectively.  $A$  is the cross-sectional area of a flux tube ( $A \propto r^3$ ).

This set of differential equations is solved numerically by the flux-corrected transport technique [Boris and Book, 1976] and are closed by using heuristic expressions for the heat flow  $q_{\parallel}$  and  $q_{\perp}$ , which closely follow the treatments in the solar wind studies [Metzler et al., 1979]. In a collisionless plasma, the usual expression for heat flow, given by  $q_{\alpha} = -K_{\alpha} \nabla T_{\alpha}$  with  $K_{\alpha}$  (where  $\alpha$  denotes  $\parallel$  or  $\perp$ ) as the thermal conductivity may not be valid because the mean free path  $\lambda \gg (T^{-1} \partial T / \partial s)^{-1}$ . In such a situation the maximum heat flow may be given by the transport of thermal energy ( $nkT_{\alpha}$ ) by the unidirectional parallel thermal velocity  $v_{th} = (kT_{\parallel} / 2\pi m)^{1/2}$  [Palmadesso et al., 1988]. Accordingly, it can be shown that (N. Singh et al., Comparison of hydrodynamic and semikinetic models for plasma flow along closed field lines, submitted to *Journal of Geophysical Research*, 1993), 1993]

$$q_{\alpha} = \epsilon \eta_{\alpha} nkT_{\alpha} v_{thi} \quad (8)$$

where  $\epsilon = -1$  if  $\partial T_{\alpha} / \partial s > 0$  and  $\epsilon = 1$  if  $\partial T_{\alpha} / \partial s < 0$ . Thus, the temperature gradient determines the sign of the heat flow but not its magnitude. The factor  $\eta_{\alpha}$  gives the reduction in heat flow due to anomalous plasma effects. In the present calculations we cannot determine the value of  $\eta_{\alpha}$  self-consistently. We study the effect of the heat flow on the results by varying the values of  $\eta_{\alpha}$ . Gombosi and Rasmussen [1991] demonstrated that in order to get realistic distribution functions from the 20-moment model, the heat flow must be small compared to the thermal speed times the pressure. In this paper,  $\eta_{\alpha} = 0$  represent no heat flow, while  $\eta_{\alpha} = 1$  corresponds to the theoretical maximum heat flow. However, since (8) is only a heuristic equation, we will take the liberty of using values for  $\eta_{\alpha}$  larger than unity to study the effect of large heat flow in a later section of this paper. Although the above expression for heat flow is a simplification it allows the inclusion of heat flow in the study rather easily and produces reliable results at least for steady state (Figure 1). As such it is used as a preliminary study before the full heat flow transport equations can be implemented.

Before we compare the results of the two models for the time-dependent cases, we shall first compare the steady state polar wind results. Figure 1 shows the density, drift velocity, parallel and perpendicular (to the direction of the magnetic field) temperatures, and parallel and perpendicular heat flows of the steady state polar wind solutions with boundary conditions given in the last section. The results of the two models show good agreement in general. The drift velocity obtained from the transport model (solid curve) is higher than that of the semikinetic model. This

discrepancy also appears later when we show the time evolution of the drift velocity. The reader should keep this in mind in subsequent comparisons.

The density, drift velocity, and perpendicular temperature of the transport model results are little affected by the choice of the heat flow parameter  $\eta_{\alpha}$  in equation (8). However, both a higher parallel and perpendicular heat flow increase the parallel temperature. We found that a value of 0.3 for both  $\eta_{\parallel}$  and  $\eta_{\perp}$  gives the closest agreement between the parallel temperature profiles of the two models. In a later section of this paper, we shall discuss in more detail the effects, on the various moments, of varying the parallel and perpendicular heat flows in a time-dependent situation.

With our particular choice of the amount of heat flow ( $\eta_{\parallel} = \eta_{\perp} = 0.3$ ), there is a cross-over at  $5.5 R_E$  for the parallel heat flow profiles from the two models. Below the cross-over the parallel heat flow in the transport model is higher than that of the semikinetic model. Both the parallel and perpendicular heat flows obtained from the semikinetic model increase sharply near the lower boundary, and then decrease with altitude above  $1.7 R_E$ . The transport model used in this particular paper failed to produce this feature. Demars and Schunk [1992] used a 16-moment transport model which produced a sharp bend in the heat flow profiles at low altitude. This could be due to the inclusion of collisions in their transport model and/or their use of the full heat flow equation to solve for  $q_{\parallel}$  and  $q_{\perp}$ . Their semikinetic model did not produce the low altitude heat flow bend when they assumed a Maxwellian velocity distribution at the boundary, but it did when the distribution was a bi-Maxwellian with zero stress. It should be noted that Demars and Schunk [1992] compared the steady state polar wind model to about  $2.9 R_E$  while a flux tube extending to  $10 R_E$  is used in this paper.

#### EXPANSION OF THE POLAR WIND INTO A LOW DENSITY PLASMA

Satellite observations indicate that the ions in the magnetosphere of ionospheric origin are much more energetic than those in the ionosphere [Baughner et al., 1980; Horwitz and Chappell, 1979]. The energization of these ionospheric ions can be explained in terms of various mechanisms, one of which is connected with the outward expansion of the topside, high-latitude ionospheric plasma along open geomagnetic field lines [Singh and Schunk, 1982, 1986]. In this section we study the time evolution of the polar wind expanding into a low density region. The study will be conducted using both the semikinetic and transport models described earlier. Our initial conditions are the same as used by Singh and Schunk [1985], who assumed a sudden drop of plasma density above a certain altitude. Note that the initial conditions we used here (and subsequent sections) may not represent real physical situations. We are mainly interested in the comparison of the results of two different models under the same conditions. Our results, however, are important to the study of the time evolution of density perturbations in space plasmas in general, irrespective of the initial boundary conditions.

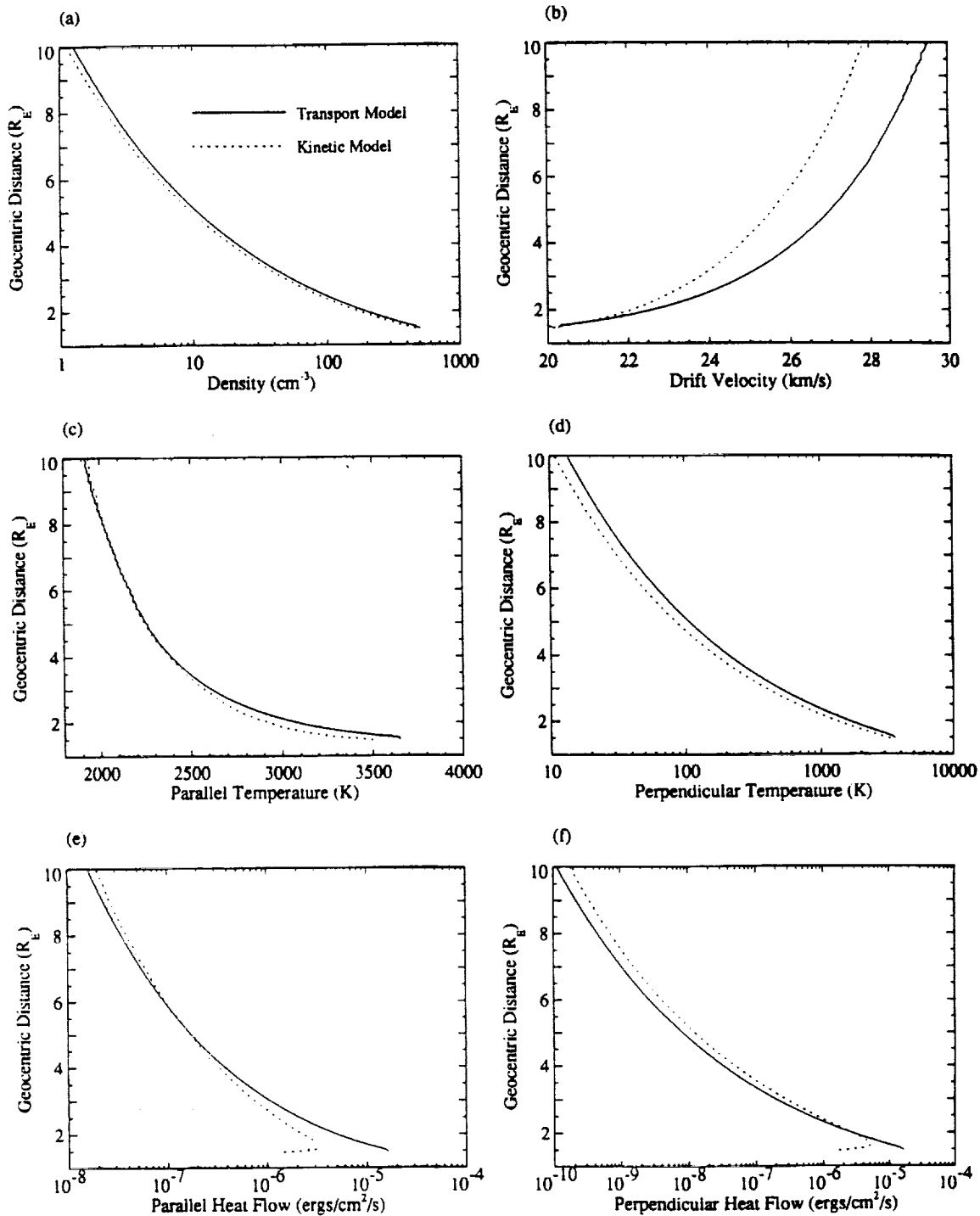


Fig. 1. Comparison of the semikinetic and hydrodynamic steady state  $\text{H}^+$  polar wind.

At time  $t = 0$ , the density of the steady state polar wind was lowered to  $0.5 \text{ ions/cm}^3$  at and above an altitude of  $9000 \text{ km}$  (density profile  $t_0$ , Figure 2a). The plasma was then allowed to evolve in time using both the semikinetic and transport models. Bulk parameters were calculated from the ion distribution function in the semikinetic model at the same selected times at which bulk parameters from the transport model were output. The transport model used for its initial conditions bulk parameters obtained from the semikinetic model at  $t_0$ . Profiles of the density,

drift velocity and parallel temperature, at different times, from both the semikinetic (dotted curves) and transport (solid curves) models are shown in Figure 2. The profiles in Figure 2 are separated by a time of 5 min.

The density profiles from both models can generally be broken down into three regions, which are indicated by  $a$ ,  $b$  and  $c$  on profile  $t_1$ . Region  $a$  ( $r < 3 R_B$ ) is the unperturbed polar wind solution, region  $b$  ( $3 - 4.5 R_B$ ) is the polar wind expansion into a region of low density plasma, and region  $c$  ( $r > 4.5 R_B$ ) is the region of low

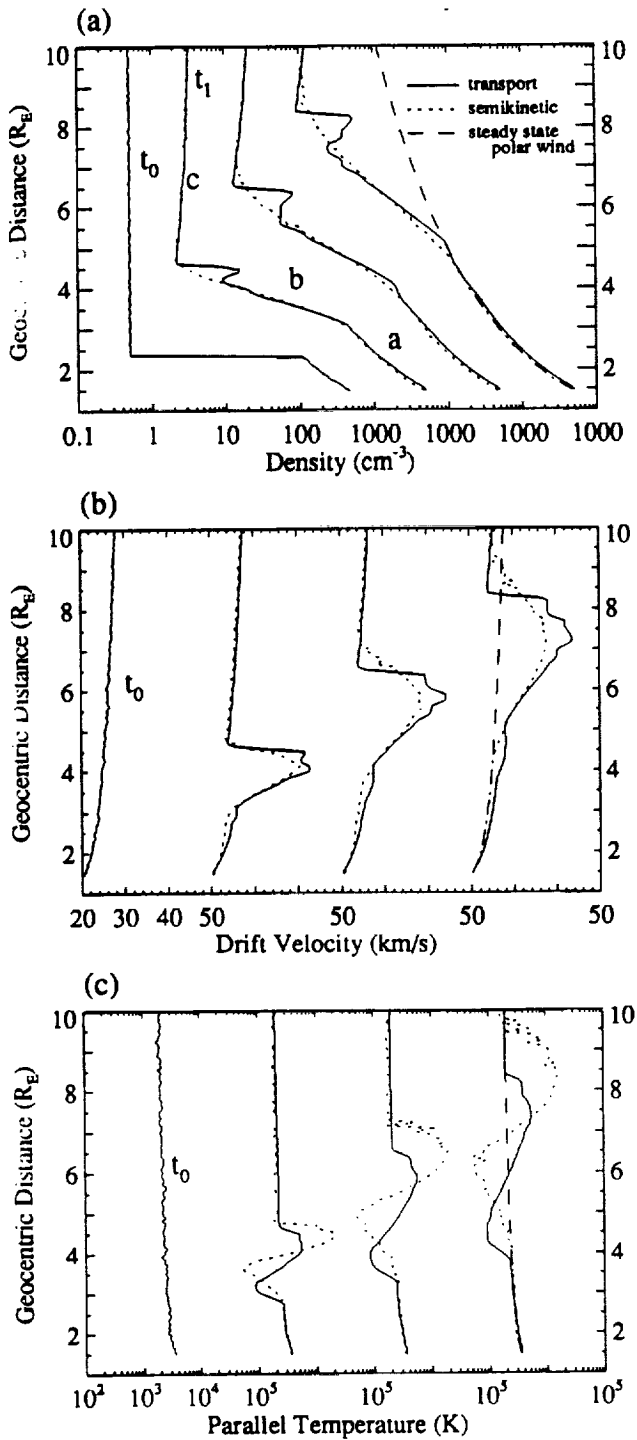


Fig. 2. Comparison of the time evolution of density, drift velocity, and parallel temperature for  $H^+$  polar wind expansion into a low-density region, from the semikinetic and transport models.  $t_0$  is the initial time, the next three profiles represent time  $t=5, 10,$  and  $15$  mins respectively.

density plasma still flowing upwards. Region a expands in altitude range as time advances because the polar wind is being continuously supplied from below the lower boundary. The perturbation propagates upward while the density profile returns to the steady state solution. As the plasma in the low density region (region c) moves upward its density decreases because

of the divergence of the flux tube. In a 15-min period the density at the upper boundary drops by about half. In region c the bulk drift velocity also decreases slightly from the steady state value because the electric field goes from being zero to being slightly negative because of the positive density gradient.

To understand the region of plasma expansion (region b), it is helpful to examine the ion distribution function. Figure 3 shows the reduced distribution function which is the ion distribution integrated over all perpendicular velocities and plotted in a phase space of parallel velocity versus radial distance. This distribution is displayed in a gray-scale format such that darker shades represent higher density. At  $t = 0$ , the electric field at the high/low-density boundary is very large because it is proportional to the initial large gradient of the density. This electric field accelerates ions in both the high- and low- density regions immediately adjacent to the density interface. These ions flow upwards and disperse in time. As they do, the density gradient and the large associated electric field diminish. Also, the dispersing ions produce a region of elevated parallel velocity, and a region where the parallel temperature is first reduced below and then elevated above the steady state temperature profile. The region of elevated drift speed is simply a result of the many high speed particles from below overtaking the slower ions above them. The region of temperature reduction occurs where ions are cooled by acceleration

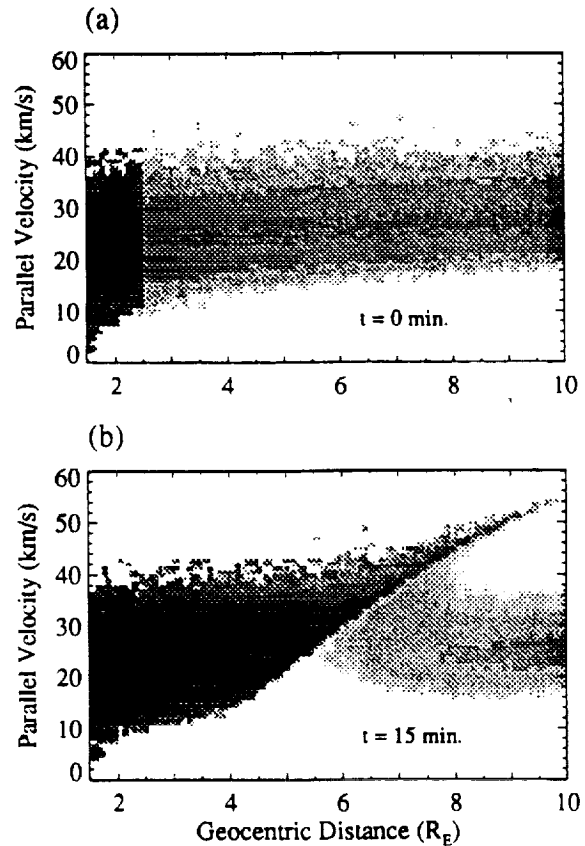


Fig. 3. Distribution function for  $H^+$  polar wind expansion into a low density region at (a)  $t=0$  and (b)  $t=15$  mins. The phase plot is in gray scale in which a darker shade represents a higher density.

through the large interface potential drop. The region of temperature enhancement develops where two ion streams exist. The altitudinal extent of each of these regions expands in time because of velocity dispersion.

The transport model results are very similar to the semikinetic model results in region *a* and *c*, but there are significant differences in the transition region *b*. A sharp and persistent density jump develops at the upper edge of this region. At the same location there is an abrupt jump in the drift velocity and parallel temperature. This shock propagates upwards with a speed of about 38 km/s which is consistent with the Rankine-Hugoniot relation [Singh and Schunk, 1985]. As this shock moves upward a local density minimum develops below it. This region of minimum density—where the maximum drift velocity and parallel temperature occur—behind a forward shock is a reverse shock [Sonett and Colburn, 1965]. Nothing corresponding to these features are seen in the semikinetic bulk parameter profiles. They are smooth and continuous throughout this region.

The parallel ion temperature obtained from the transport model also has a leading elevated value and a trailing suppressed value; however, this wave feature moves up the flux tube more slowly than the similar feature seen in the semikinetic temperature results. Velocity dispersion plays an important role in creating this difference. The first ions to reach a given altitude are ions with high velocity. When they first arrive, however, they make up only a small fraction of the total number of ions present. Their contribution to the local bulk moments become more pronounced as their velocity, raised to increasing powers, starts to outweigh

their small relative numbers. One would then expect to see increasing disagreement among transport and semikinetic model moments with increasing moment order, to the degree to which the transport model does not properly describe the effects of velocity dispersion. In the case under discussion here, the disagreement is quite pronounced starting at the parallel temperature moment.

The shock in the results of the transport model in Figure 2 can be seen as discontinuous jumps in the density, drift velocity, and parallel temperature. Clearly, the values of all three of these moments are tightly coupled at the location of the shock. In figure 4a one can see the density, drift speed and parallel temperature profiles from the transport model at  $t = 15$  min. In addition to the correlation among the moments evident at the shock, other instances of correlation (such as the point where the maximum drift speed and parallel temperature occur) can be seen. This correlation is, of course, a consequence of the coupled nature of the differential equations in the transport model. The semikinetic model results display no such correlation among the moments as can be seen in the profiles in figure 4b. This is a consequence of phase mixing where kinetic effects damp waves generated by the initial perturbation. In the transport model such waves persist because the truncated moment set does not allow phase mixing.

The temperature elevation of the semikinetic model (e.g., between 7 and 10  $R_E$  at  $t = 15$  min in Figure 2c) is the "effective temperature" that results when the ions in the low density region and the ions in the high speed stream are counted as one population. Such "effective

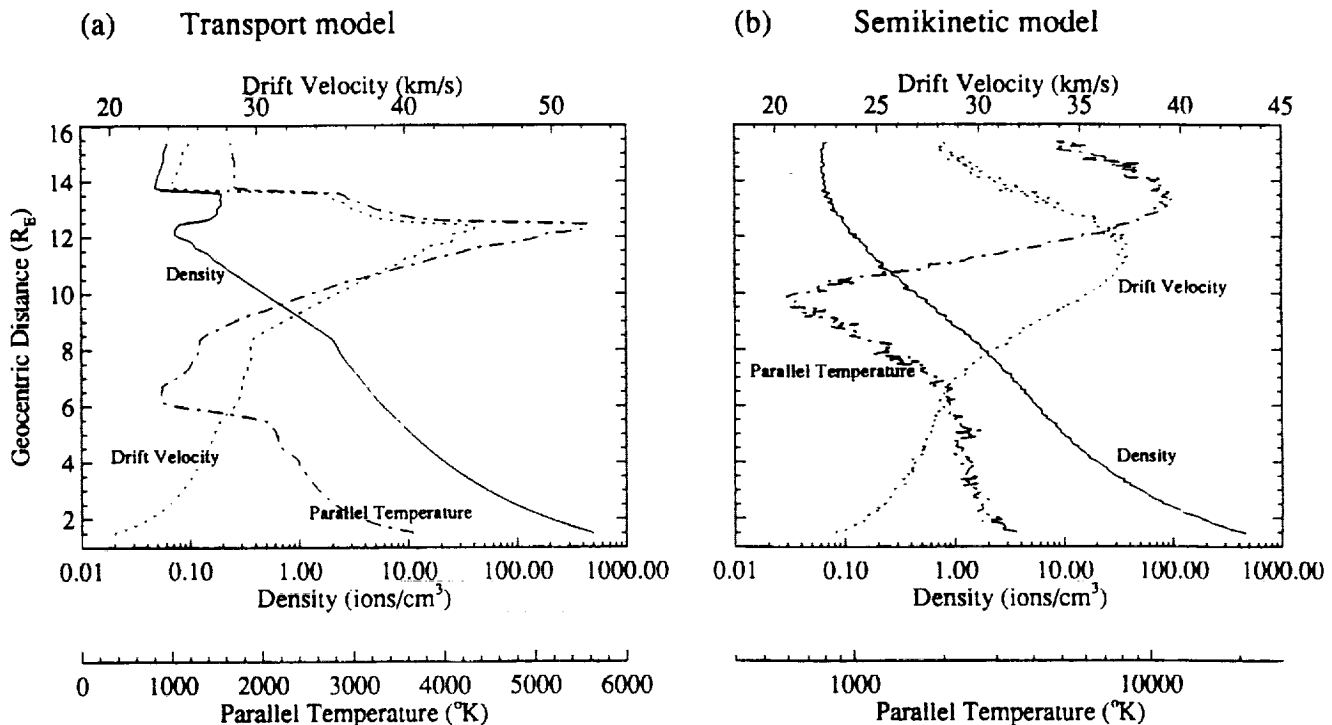


Fig. 4. Comparison of density, drift velocity and parallel temperature of the (a) transport and (b) semikinetic model at  $t=15$  mins for the case of  $\text{H}^+$  polar wind expansion into a low-density region. Note that the transport model profiles have a one-to-one correspondence in their local minima and maxima.



temperature" is not found in the transport results when only one ion stream is simulated. Multistream fluid codes can be implemented for streams originating from specified sources, however, such codes cannot model plasmas which develop multiple streams during the course of the simulation, unless the locations and times where such streams will develop can be anticipated.

Like the density profile, parallel heat flow (parallel thermal energy per unit area per unit time) shows a sudden drop at about  $2.4 R_B$  at  $t = 0$  when the perturbation is first imposed (not shown). However, the parallel and perpendicular heat flow per ion retain the same profile at  $t = 0$  as that of the steady state polar wind because the distribution function remains exactly the same as the steady state polar wind at  $t = 0$  except for a uniform number density above  $2.4 R_B$ . (In the following we shall restrict our discussion to the heat flow per ion as it is found to be more illuminating.) Figure 5 shows the parallel heat flow per ion at time  $t = 15$  min. The semikinetic profile (dotted curve) has a negative heat flow from about  $6.2$  to  $8.1 R_B$  which corresponds to the positive slope of the parallel temperature as seen in Figure 4b. It also has positive heat flow above and below this region where the parallel temperature has a negative slope. One can see from this that the semikinetic results support the idea that the sign of the heat flow depends on the sign of the slope of the temperature, as used in the transport model formulation (Equation (8)).

The parallel heat flow calculated from the transport model (solid curve) also has a local minimum and maximum around  $7.4 R_B$ . The direction of the heat flow is determined by the slope of the parallel temperature as required by (8). The magnitude of the local minimum and maximum heat flow is about an order of magnitude less than that obtained from the semikinetic model.

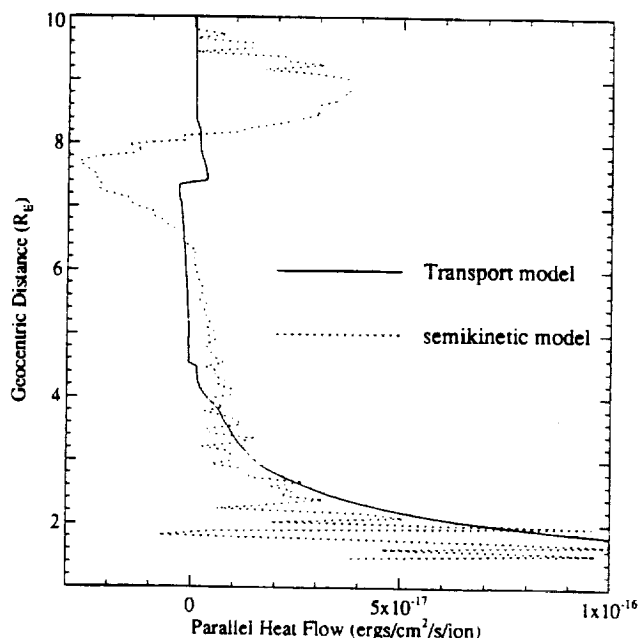


Fig. 5. Comparison of the parallel heat flow of the semikinetic and transport model at  $t=15$  mins for the case of  $H^+$  polar wind expansion into a low-density region.

An increase of  $\eta_\alpha$  in (8) will make the comparison of the heat flow of the two models more favorable. Later on, we shall see that a larger heat flow will result in a better agreement of the lower moments also. The reader should bear in mind that the value of  $\eta_\alpha$  use here ( $\eta_\alpha = 0.3$ ) was chosen so that the steady state solutions of both models would be as close as possible. The effect of varying  $\eta_\alpha$  on the transport model results, will be discussed later.

#### EVOLUTION OF A LOCALIZED DENSITY ENHANCEMENT

The Earth-space environment is a region of dynamic plasma phenomena. Both heavy and light ions are created and destroyed through photoionization and charge exchange in the ionosphere, and are continuously transported throughout the magnetosphere. One should therefore expect to find regions in the magnetosphere where the plasma densities are high and regions of relatively low density. For instance, density enhancements at high altitude could arise from electric field heating at low altitudes [Hultqvist, 1991] followed by the upward propagation of the hot plasma to higher altitudes. Recently Singh [1992] has shown that plasma enhancements and cavities can be created by transverse ion heating via wave-particle interactions. In this section, we will investigate the time evolution of a localized plasma density enhancement in the classical supersonic  $H^+$  polar wind.

The density of the imposed plasma enhancement is given at time  $t = 0$  by

$$n_{enh}(r) = pn_{pw}(r)e^{-\frac{1}{2}\left(\frac{r-r_p}{\sigma}\right)^2} \quad (9)$$

where  $n_{pw}(r)$  is the steady state polar wind density.  $n_{enh}(r)$  is therefore a Gaussian distribution along  $r$  with a peak value of  $p$  times  $n_{pw}$  at  $r = r_p$ . We chose  $p$ ,  $\sigma$  and  $r_p$  to be 5, 1260 km and 15600 km respectively. The plasma density enhancement has zero flow velocity initially and has an ion temperature of 500 K for both  $T_{||}$  and  $T_{\perp}$ .

The density, flow velocity and parallel temperature of the semikinetic model at  $t = 0$ , when the density enhancement was first introduced, are given in Figures 6a, 6b and 6c and are marked by  $t_0$  (Dotted curve). Again, the plasma distribution function in parallel velocity and radial distance phase space, as shown in Figure 7, are used to interpret the various bulk parameters. The stationary plasma density enhancement causes the net bulk velocity to decrease to about 4 km/s at the peak of the density enhancement, compared to 23 km/s for the steady state polar wind (dashed curves). The double peak in the parallel temperature profile at  $t = 0$  can be explained in the following way. When nearly equal populations with a relative drift exist, the parallel temperature will be associated with the separation, in velocity space, of these populations. When either population is dominant, the temperature will be approximately that of the dominant population. At 2 and  $2.8 R_B$  the density of the imposed plasma population is comparable to that of the polar wind. At the center of the imposed population, at  $2.4 R_B$ , the imposed ion density exceeds the polar wind background

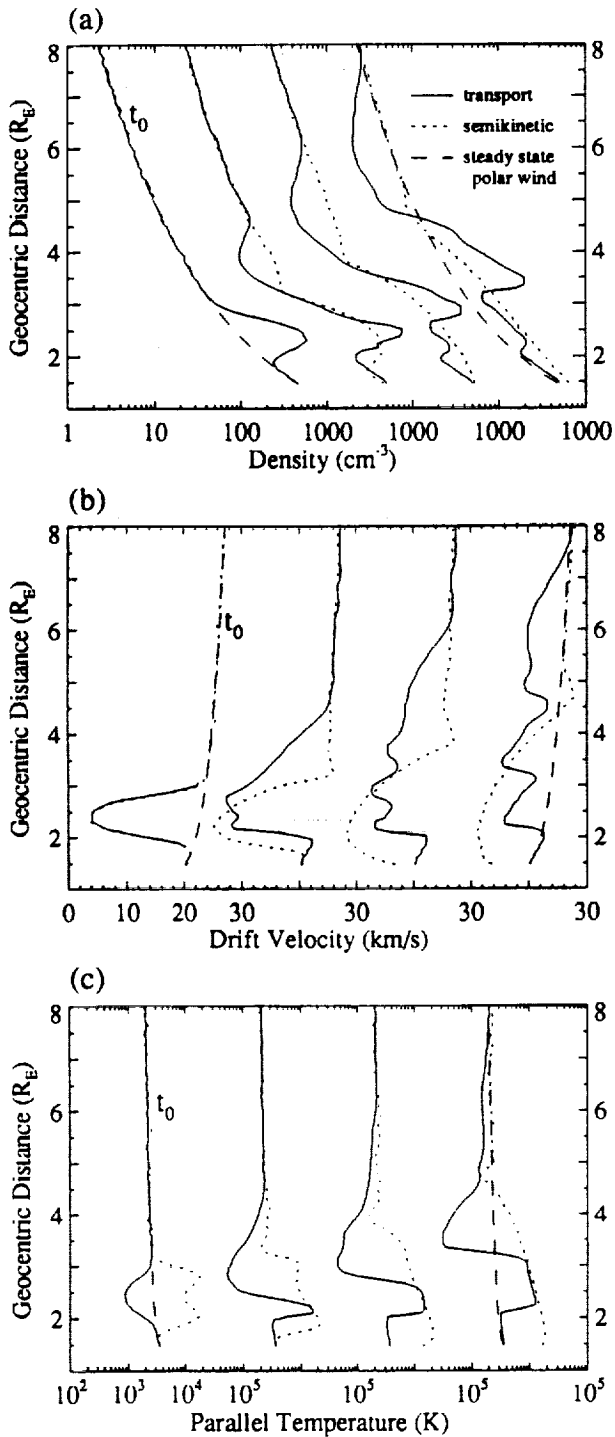


Fig. 6. Comparison of the time evolution of density, drift velocity and parallel temperature for a cold density enhancement in the  $H^+$  polar wind from the semikinetic and transport models. The initial conditions for the drift velocity and parallel temperature in the transport model are calculated by using equations (10) and (11). The parallel temperature, according to the transport model, decreases at the location of the density enhancement, opposite to what occurs in the semikinetic model.

density. Where these two different populations have near equal numbers the effective temperature is the highest. At points where one dominates the other the effective temperature tends toward that of the dominant population.

The density profiles obtained by the semikinetic model (dotted curves, Figure 6a) show that the density enhancement flattens out with time. This is due in large part to the distribution of ion velocities (both positive and negative) in the density enhancement. This dispersal flattening of the density enhancement can be seen in the phase plot in Figure 7b where the density enhancement is now very elongated. The electric field modifies the dispersion of the enhancement because above and below the density peak it has opposite signs (as a result of opposite density gradients). Above the peak it is positive and accelerates the ions upward, while below the peak it is negative and accelerates the ions downward. The downward flowing ions increase the density of the plasma at the lower boundary, and lower somewhat the flow velocity of the plasma.

In comparing with the results of the semikinetic model in a consistent manner, one could use in the transport model the same initial bulk parameter profiles as produced by the semikinetic model. However, in a single-fluid treatment, the initial parallel temperature profile of the semikinetic model would be interpreted as a warm density enhancement. In order to find out how a cold density enhancement would evolve under a hydrodynamic treatment, we use the transport model with initial conditions established by the usual definitions for a single fluid:

$$\bar{v} = \frac{n_0 v_0 + n_1 v_1}{n_0 + n_1} \quad (10)$$

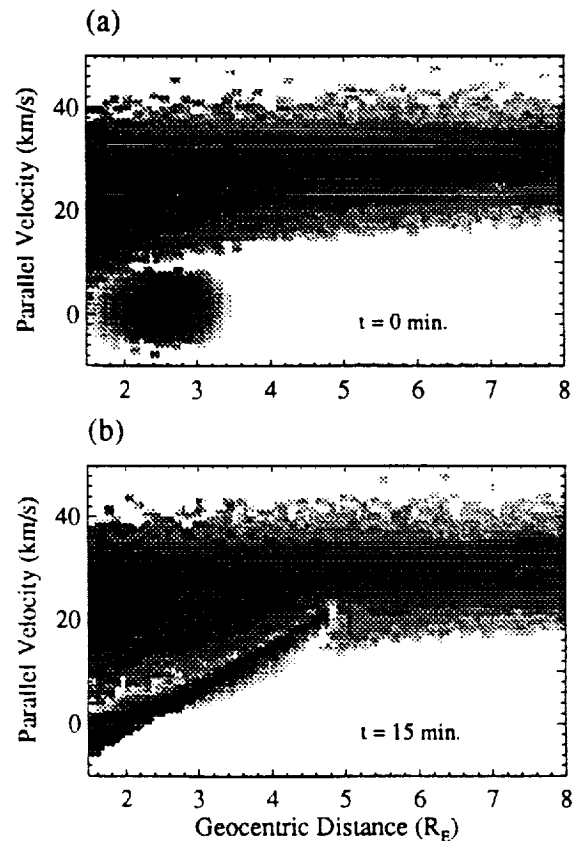


Fig. 7. Distribution function for a density enhancement in the  $H^+$  polar wind at (a)  $t=0$  and (b)  $t=15$  mins. The phase plot is in gray scale in which a darker shade represents a higher density.

$$\bar{T}_\alpha = \frac{n_0 T_{\alpha 0} + n_1 T_{\alpha 1}}{n_0 + n_1} \quad (11)$$

where  $\bar{v}$  and  $\bar{T}_\alpha$  are the average flow velocity and ion temperature and  $\alpha$  stands for  $\parallel$  or  $\perp$ . The "0" subscript denotes the polar wind while the "1" subscript indicates parameters of the density enhancement. In (10) and (11),  $n_1 = n_{enh} - n_{pw}$ ,  $v_1 = 0$  and  $T_{\alpha 1} = 500$  K. These initial profiles are shown in Figure 6 (solid curve,  $t = 0$ ). The velocity profile at  $t = 0$  obtained from (10) is very close to the semikinetic model initial profile, however, the parallel temperature profile at  $t = 0$  has a minimum value at the peak of the density enhancement which indicates that the density enhancement is cold.

It is necessary to point out that the discrepancies of the two models at the lower boundary are due to the difference between the way the boundary conditions are handled in each case. In the transport model the density, the drift speed, and the parallel and perpendicular temperatures have specified unchanging values at the lower boundary. In the semikinetic model only the distribution of upgoing ions at the lower boundary is held fixed. The velocity distribution of downgoing ions at the lower boundary is determined by what happens at the flux tube, and as a result, will change with time. The moments found from integrations over the total velocity distribution (upgoing and downgoing ions) will also change. The increase in the density, the drop in the drift speed and the rise in the parallel temperature seen in the semikinetic results at the lower boundary result from part of the ions from the density enhancement population falling out of the base of the flux tube.

In the various transport bulk parameter profiles seen in Figure 6 a number of small scale features develop. The number of these features increases with time. They are also seen to move upward with varying speeds. Although we have not done the wave analysis of the transport model used in this paper, we believe that these features result because of the excitation of several fundamental wave modes by the initial perturbation. (It is likely that these wave modes will be different from those discussed by Gombosi and Rasmussen [1991] because of differences between the transport model used in this paper and the 20-moment expansion of Gombosi and Rasmussen.) Differences in the phase velocity of the different modes lead to the development of increasing numbers of small-scale features. If a transport model solving the heat flow equations were used the solution would change no doubt; the old wave modes would be modified and new ones would be introduced. Since the semikinetic results do not develop the same small scale features as are produced by the generalized transport model used in this paper, it is clear that most of these wave modes are spurious. Phase mixing in the semikinetic model is responsible for their elimination.

We have also compared with the semikinetic results, the results from the transport model when its initial parameter profiles are taken to be the same as those produced by the semikinetic model at  $t = 0$  [Ho et al., 1993]. Although in this case, an imposed cold plasma (semikinetic) and a warm plasma (transport) are compared, it is interesting to note that the re-

sults are closer than the case when a cold plasma enhancement (according to equations (10) and (11)) is used. Furthermore, Ho et al. [1993] show that when a strong heat flux was induced artificially by increasing the value of  $\eta_\alpha$  in (8), the shocks are eliminated and the results of the transport and semikinetic models are much closer.

#### EVOLUTION OF A LOCALIZED DENSITY CAVITY

In this section, we study the time evolution of a localized density cavity in the steady state  $H^+$  polar wind. The cavity was created by decreasing the density of the plasma along  $r$  by

$$n_{cav}(r) = pn_{pw}(r)e^{-\frac{1}{2}\left(\frac{r-r_p}{\sigma}\right)^2} \quad (12)$$

where  $p = 0.9$ ,  $\sigma$  and  $r_p$  have the same meaning and values as in case of the density enhancement (1260 and 15,600 km respectively). The density profile  $t_0$  in Figure 8a is therefore given by

$$n(r) = n_{pw} - n_{cav} \quad (13)$$

where  $n_{pw}$  is the density of the steady state polar wind. Since the ion distribution is unchanged, the velocity and parallel temperature at  $t = 0$  when the cavity is created are the same as that of the steady state polar wind ( $t_0$ , Figures 8b and c).

For the semikinetic model, the cavity propagates upward, becomes less deep, and extends over a larger altitude range in time. The cavity propagates with an average speed of about 30 km/s. From the ion distribution function (Figure 9), the cavity is seen to lean towards the abscissa in time. This is again due to velocity dispersion and explains the spreading out of the cavity in time.

The drift velocity and the parallel temperature profiles can also be readily interpreted by inspecting the ion distribution function. For instance, at  $t = 15$  min, the reduced number of low-velocity ions near  $5 R_E$  (Figure 9b) causes a higher bulk velocity at that altitude, while the loss of ions at the high-velocity end around  $7 R_E$  causes a lower bulk velocity there. The resultant velocity profile is a rounded double-sawtooth structure (Figure 8b, dotted curve).

At  $t = 15$  min, the parallel velocity distribution function at  $4.5 R_E$  and  $7.5 R_E$  is narrower than at other altitudes which results in lower parallel temperatures there. Note that the locations where the velocity has a local minimum and maximum do not occur at the same altitudes as where the parallel temperature minima occur. (In the transport model results these locations do line up.) Sandwiched between the two low temperature regions is a region of higher temperature (about 1.6 times that of the steady state polar wind). The high temperature is a result of the double-humped distribution formed by the cavity seen in the phase space plot (Figure 9b). These structures, in both the velocity and parallel temperature profiles, propagate upward in time and become less sharply defined due to ion dispersion.

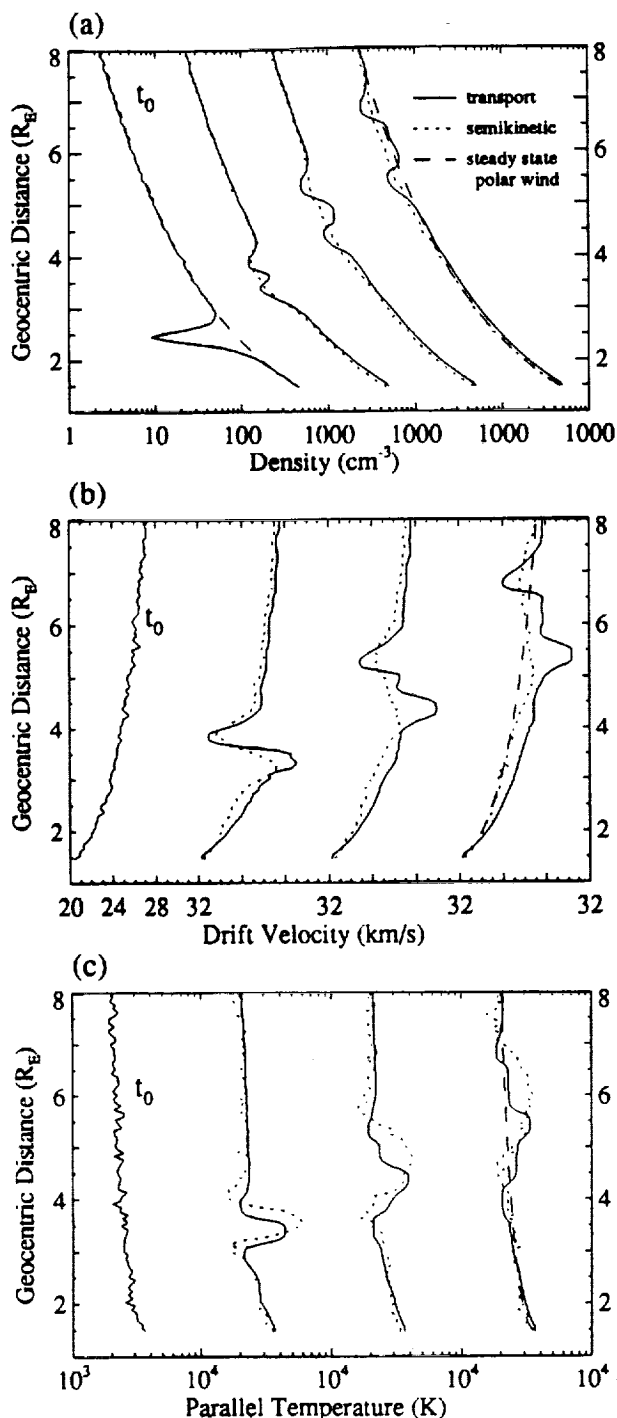


Fig. 8. Comparison of the time-evolution of density, drift velocity, and parallel temperature for a density cavity in the  $H^+$  polar wind, from the semikinetic and transport models. Here  $t_0$  is the initial time, the next three profiles represent time  $t=5, 10,$  and  $15$  minutes respectively.

The density profiles from the transport model are significantly different. Figure 8a (solid curves) show that within 5 min after the local density cavity has been created, the cavity is being filled with ions to form two separate cavities. These cavities propagate upwards with speeds of 22 and 33 km/s, respectively, getting further and further apart. The velocity profiles of the transport model also develop a double saw-tooth structure as in the semikinetic case. However, the

velocity enhancement (lower "tooth") and depression (upper "tooth") are separated more and more in time and are linked by a region where the velocity returns to the unperturbed steady state value. It is important to note that the location of the velocity enhancements and depressions correspond to the secondary cavities in the transport model results while for the semikinetic model they correspond to the inner walls of the original cavity. Note also that the overall discrepancy of the velocity profiles of the two models at later time is due to the discrepancy of the two models in flow velocity in steady state (see Figure 1b). The time-dependent behavior of a cavity in a plasma obtained by the transport model is similar to the results of Singh and Schunk [1985].

Figure 8c compares the parallel temperature of the cavity in the polar wind obtained by both the semikinetic and transport models. In comparison to the semikinetic model, the parallel temperature of the transport model shows the same structure of a high temperature region sandwiched between two low temperature regions. However, the transport model parallel temperature does not spread out as much and the low and high temperature regions remain distinct with magnitudes that decrease with time.

EFFECT OF HEAT FLOW ON THE TRANSPORT MODEL RESULTS

The values for  $\eta_{||}$  and  $\eta_{\perp}$  used for the heat flow in (8) for all the cases we have studied so far is 0.3. This

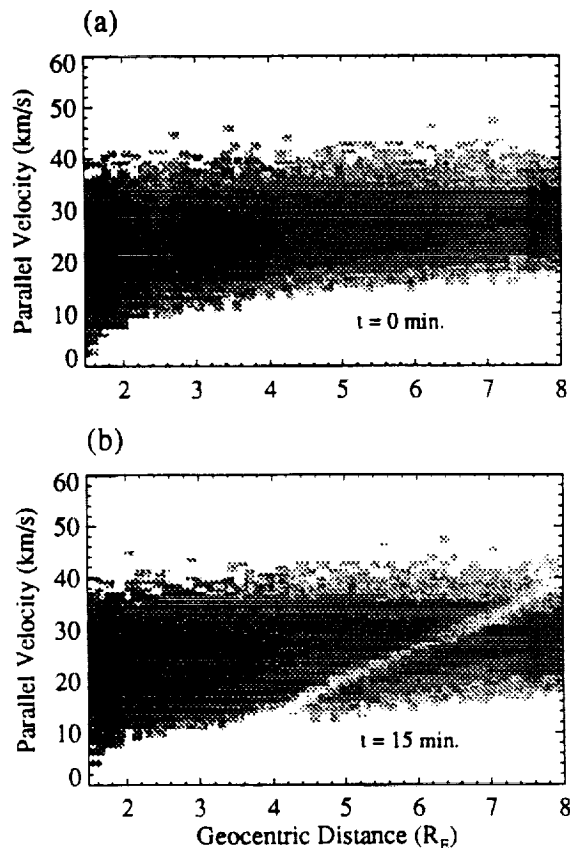


Fig. 9. Distribution function of a density cavity in the  $H^+$  polar wind at (a)  $t=0$  and (b)  $t=15$  mins. The phase plot is in gray scale in which a darker shade represents a higher density.

Geocentric Distance ( $R_E$ )

Fig. for model diff of t

val and stat neg the excl cau to t at s per par was whi

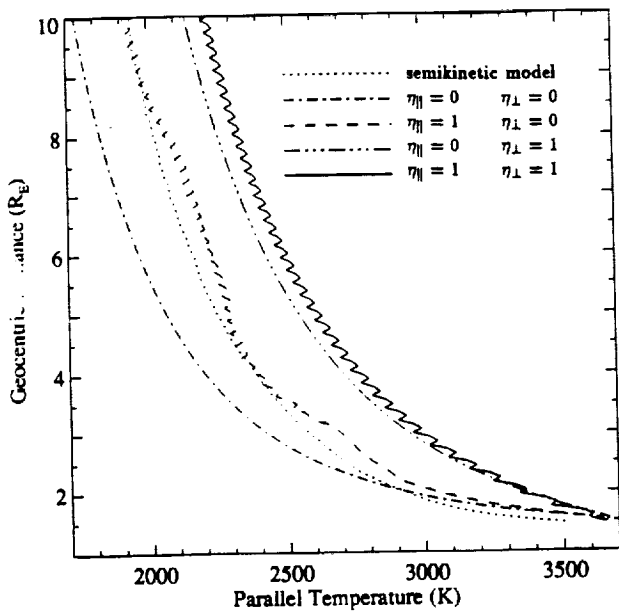


Fig. 10. Steady state H<sup>+</sup> polar wind parallel temperature for different heat flows. The dotted curve is the semikinetic model results and the other curves are obtained by using different values of  $\eta_{\parallel}$  and  $\eta_{\perp}$  (as indicated) in equations (8) of the transport model.

value gave the best comparison between the semikinetic and transport models at steady state. For steady state, the amount of heat flow was found to have a negligible effect on all of the bulk parameters except the parallel temperature. Figure 10 shows that the exclusion of heat flow in the transport model ( $\eta_{\alpha} = 0$ ) causes the parallel temperature (dotted-dashed curve) to be lower than the semikinetic model (dotted curve) at steady state. We found that both the parallel and perpendicular heat flow can increase the polar wind parallel temperature. When  $\eta_{\parallel} = 1$ ,  $T_{\parallel}$  (dashed curve) was brought close to the curve of the semikinetic model, while  $\eta_{\perp} = 1$  alone yields an even higher  $T_{\parallel}$  (dashed-

dotted-dotted-dotted curve). When both  $\eta_{\parallel}$  and  $\eta_{\perp}$  equal one the highest  $T_{\parallel}$  (solid curve) results. It is about 500 K higher at the upper boundary than the case without heat flow. The fact that  $q_{\perp}$  can affect  $T_{\parallel}$  can be seen from equation (6), in which the last term converts transverse energy to parallel energy by means of the mirror force. In comparison with the  $q_{\parallel}$  term,  $q_{\perp}$  has a larger effect on  $T_{\parallel}$  because the term which is dependent on  $q_{\parallel}$  in equation (6) can be broken down into a negative and positive term. The negative term decreases  $T_{\parallel}$  for increasing  $q_{\parallel}$ , while the positive term is proportional to  $\partial q_{\parallel} / \partial s$ , and has a magnitude smaller than the term which depends on  $q_{\perp}$ .

Although the amount of heat flow has effects only on the parallel temperature at steady state, we found that it can greatly affect various other bulk parameters in a time-dependent situation. By increasing the heat flow the sharpness of the shocks is reduced and smoother bulk parameter profiles are produced. This can be seen from Figure 11 which shows the density and parallel temperature for different heat flow parameters  $\eta_{\alpha}$ , at a time of 15-min after the density enhancement was imposed on the steady state H<sup>+</sup> polar wind. When  $\eta_{\parallel}$  and  $\eta_{\perp}$  both equal 1 the shocks produced by the density enhancement are reduced in comparison to the case when there is no heat flow (dashed curve in comparison to dashed-dotted curve, Figure 11). We have seen from Figure 5 that the heat flow from the semikinetic model can be about an order of magnitude larger than that of the transport model when  $\eta_{\parallel}$  and  $\eta_{\perp}$  is taken to be 0.3. By using large values of  $\eta_{\parallel}$  and  $\eta_{\perp}$  (7.5 for the solid curves in Figure 11), the heat flow obtained from the transport model is increased by 25 times, and the magnitudes of the heat flow from the two models are closer.

In allowing  $\eta_{\parallel}$  and  $\eta_{\perp}$  to be larger than 1 we have violated the original assumption that the heat flow cannot be larger than the pressure times the thermal speed [Gombosi and Rasmussen, 1991]. However, since (8) is only a heuristic formula, there is in practice

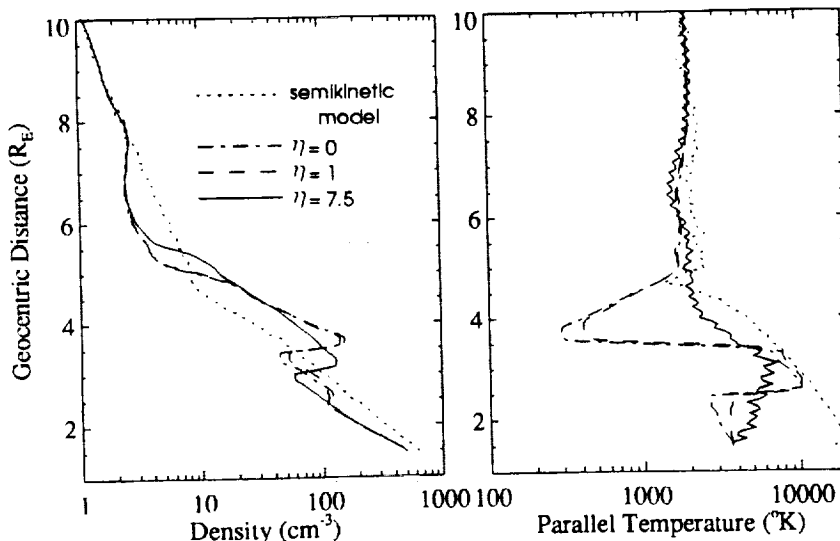


Fig. 11. Density and parallel temperature from the semikinetic model (dotted curve) and the transport model with  $\eta_{\parallel}$  and  $\eta_{\perp}$  given the value of 0 (dot-dashed curve), 1 (dashed curve), and 7.5 (solid curve). These profiles are for a density enhancement case at  $t=15$  min.

no limit on the magnitude of  $\eta_{\parallel}$  and  $\eta_{\perp}$ . It is shown in Figure 11 that the sharp gradient structures of the transport model profiles are reduced when increasing values of  $\eta_{\parallel}$  and  $\eta_{\perp}$  are used. The results obtained by the transport model for large heat flow are closer to those of the semikinetic model. There are situations when the hydrodynamic shocks can be totally dissipated by a large heat flow, this is found in the case of a warm plasma imposed in the polar wind [Ho *et al.*, 1993].

The values of the heat flow parameters  $\eta_{\parallel}$  and  $\eta_{\perp}$  which were chosen to give a favorable comparison between the transport model and the semikinetic model at steady state have been shown to be too small for a evolving cold plasma density enhancement. This implies that a more sophisticated form of heat flow equations such as the full heat flow transport equation may be needed for a more accurate comparison. The results obtained in the present study, however, give strong evidence that heat flow, or even higher-order moments, are able to reduce the sharp gradient features of the transport model profiles. This should be true regardless of the form of the heat flow equation being used.

#### DISCUSSION AND CONCLUSION

Closing the set of equations in the transport model by use of an heuristic heat flow expression, we have shown, as have Demars and Schunk [1992], that the transport and semikinetic models agree reasonably well up through the heat flow moments, in steady state with supersonic flow. However, for time-dependent situations, drastic disagreements occur, even for the lowest-order moments. One of the main differences between the two models is the development of shock fronts in the transport model. The semikinetic model produces smooth profiles in general, and the initial perturbation in the density and the other bulk parameters smooths out and diminishes in magnitude with time, returning rapidly to the steady state solution. Another difference between the results of the two models is that the correlation between the location of local maxima and minima seen in the results of the transport model are not seen in the semikinetic model. Additionally, the transport model may, under certain circumstances, develop various small scale features which are not seen in the semikinetic results. One of the main reasons for these differences is that the semikinetic model properly includes the effects of velocity dispersion up through the higher velocity moments. It also includes the process of phase mixing, which is a thermal wave damping mechanism [Palmadesso *et al.*, 1988], which acts to smooth profiles and eliminate small-scale features.

In examining the general structure of various bulk parameters obtained by the two models, the fact that the semikinetic results are smoother as a result of velocity dispersion and phase mixing leads to the argument that the shocks seen in the transport model results are an artificial consequence of the lack of these processes in the transport model. Without the cross boundary relief that these two processes provide, the density, velocity and temperature of two

adjacent regions can maintain very different values (i.e., a shock front). This view is supported by the fact that the results of the transport model are smoother when a higher heat flow is introduced artificially. One may argue that the discrepancies between the semikinetic and transport models may be due partly to the inability of equation (8) to properly describe the heat flow, and that therefore, the heat flow equations should be included in the transport model equation set. As discussed by Palmadesso [1988] and Gombosi and Rasmussen [1991], such a higher order model would still generate spurious waves since it lacks the higher moments needed to include full phase mixing. However, the solutions from such a model would differ somewhat from the transport model results presented in this paper, and might be closer to those of the semikinetic approach.

Much of the difference between the results of these two models is due to the fact that the transport model encounters difficulty in handling multi-streaming ion distributions. Although transport equations can be formulated to simulate multiple ion streams, this approach is useful only when the origin of the ion streams are known in advance. In many time-dependent situations, processes in the evolving system generate separate streams. The semikinetic model handles the development of these streams naturally.

One of the attractive features of the semikinetic model is that the additional information contained in the velocity distribution function makes it very easy to understand why certain features are seen in the bulk parameter profiles. For example, the increase in bulk velocity in a certain region is usually due to the presence of high-velocity ions, as in the plasma expansion into a low density region case, or due to the reduction of low-velocity ions as in the propagation of an ion depleted region case. On the other hand, the decrease of bulk velocity could be due to the presence of a second stream of low-velocity plasma, as in a density enhancement case, or the reduction of high-velocity ion as in the density cavity case. In the same way, the elevation of the ion temperature in various regions is often due to the presence of a second stream of ions and the depression of the temperature can be a consequence of the narrowing of the velocity distribution in these regions or the presence of a dominant low temperature population.

*Acknowledgments.* This research is supported under NASA grant NAG8-134, NAG8-822, NAG8-239, NAGW-1554 and NGAW-2903.

The Editor thanks C. E. Rasmussen and another referee for their assistance in evaluating this paper.

#### REFERENCES

- Banks, P. M., and T. E. Holzer, The polar wind, *J. Geophys. Res.*, **73**, 6848, 1968.
- Banks, P. M., and T. E. Holzer, Features of plasma transport in the upper atmosphere, *J. Geophys. Res.*, **74**, 6304, 1969.
- Barakat, A. R., and R. W. Schunk, O<sup>+</sup> ions in the polar wind, *J. Geophys. Res.*, **88**, 7887, 1983.
- Baughar, C. R., C. R. Chappell, J. L. Horwitz, E. G. Shelley, and D. T. Young, Initial thermal Plasma observation from ISEE 1, *Geophys. Res. Lett.*, **7**, 657, 1980.

- Boris, J. P., and D. L. Book, Solution of continuity equations by the method of flux-corrected transport, *Methods Comput. Phys.*, **16**, 85, 1976.
- Brown, D. G., G. R. Wilson, and J. L. Horwitz, and D.L. Gallagher, 'Self-consistent' production of ion conics on return current region auroral field lines: A time-dependent, semi-kinetic model, *Geophys. Res. Lett.*, **18**, 1841, 1991.
- Demars, H. G., and R. W. Schunk, Semikinetic and transport models of the polar and solar winds *J. Geophys. Res.*, **97**, 1581, 1992.
- Essler, A. J., and P. A. Cloutier, Discussion of letter by Peter M. Banks and Thomas E. Holzer, 'The polar wind,' *J. Geophys. Res.*, **74**, 3730, 1969.
- Donahue, T. M., Polar ion flow: Wind or breeze?, *Rev. Geophys. Space Phys.*, **9**, 1, 1971.
- Ganguli, S. B., and P. J. Palmadesso, Plasma transport in the auroral return current region, *J. Geophys. Res.*, **92**, 8673, 1987.
- Ganguli, S. B., H. G. Mitchell, and P. J. Palmadesso, Behavior of ionized plasma in the high latitude topside ionosphere: The polar wind, *Planet. Space Sci.* **35**, 703, 1987.
- Gombosi, T. I., and A. F. Nagy, Time-dependent polar wind modeling, *Adv. Space Res.*, **8**, 59, 1988.
- Gombosi, T. I., and C. E. Rasmussen, Transport of gyration dominated space plasmas of thermal origin, 1, Transport equations, *J. Geophys. Res.*, **96**, 7759, 1991.
- Ho, C. W., J. L. Horwitz, N. Singh, T. E. Moore, and G. R. Wilson, Effects of magnetospheric electrons on polar plasma outflow: A semikinetic model, *J. Geophys. Res.*, **97**, 8425, 1992.
- Ho, C. W., J. L. Horwitz, N. Singh, and G. R. Wilson, Comparison of transport and semikinetic model: prediction for evolution of a density enhancement in the polar wind, in *Physics of Space Plasmas (1992)*, SPI Conference Proceedings and Reprint Series, Number 12, T. Chang, G. B. Crew, and J. R. Jasperse, eds. (Scientific Publishers, Cambridge, Mass., 1993), in press.
- Holzer, T. E., J. A. Fedder, and P. M. Banks, A comparison of kinetic and hydrodynamic models of an expanding ionosphere, *J. Geophys. Res.*, **76**, 2453, 1971.
- Horwitz, J. L., Parabolic heavy ion flow in the polar magnetosphere, *J. Geophys. Res.*, **92**, 175, 1987.
- Horwitz, J. L., and C. R. Chappell, Observations of warm plasma in the dayside plasma trough at geosynchronous orbit, *J. Geophys. Res.*, **84**, 7075, 1979.
- Horwitz, J. L., and M. Lockwood, The cleft ion fountain: A two-dimensional kinetic model, *J. Geophys. Res.*, **90**, 9749, 1985.
- Hultqvist B., Extraction of ionospheric plasma by magnetospheric processes, *J. Atmos. Terr. Phys.*, **53**, 3, 1991.
- Lemaire, J., and M. Scherer, Model of the polar ionosphere, *Planet. Space Sci.*, **18**, 103, 1970.
- Lemaire, J., and M. Scherer, Simple model of the polar ionosphere in an open magnetic field, *Phys. Fluids*, **14**, 1683, 1971.
- Li, P., G. R. Wilson, J. L. Horwitz, and T. E. Moore, Effect of mid-altitude ion heating on ion outflow at polar latitudes, *J. Geophys. Res.*, **93**, 9753, 1988.
- Metzler, N., S. Cuperman, M. Dryer, and P. Rosenau, A time-dependent two-fluid model with thermal conduction for the solar wind, *Astrophys. J.*, **231**, 960, 1979.
- Marubashi, K., Escape of the polar-ionospheric plasma into the magnetospheric tail, *Rep. Ionos. Space Res. Jap.*, **24**, 332, 1970.
- Palmadesso P. J., S. B. Ganguli, and H. G. Mitchell, Jr., Multimoment fluid simulations of transport processes in the auroral zones, in *Modeling Magnetospheric Plasma*, *Geophys. Monogr. Ser.*, vol. 44, edited by T. E. Moore and J. H. Waite, p. 133, AGU, Washington, D. C., 1988.
- Mitchell, H. G., and P. J. Palmadesso, A dynamic model for the auroral field line plasma in the presence of field-aligned current, *J. Geophys. Res.*, **88**, 2131, 1983.
- Schunk, R. W., and D. S. Watkins, Electron temperature anisotropy in the polar wind, *J. Geophys. Res.*, **86**, 91, 1981.
- Singh, N., Plasma perturbations created by transverse ion heating events in the magnetosphere, *J. Geophys. Res.*, **97**, 4235, 1992.
- Singh, N., and R. W. Schunk, Numerical calculations relevant to the initial expansion of the polar wind, *J. Geophys. Res.*, **87**, 6487, 1982.
- Singh, N., and R. W. Schunk, Temporal evolution of density perturbations in the polar wind, *J. Geophys. Res.*, **90**, 6487, 1985.
- Singh, N., and R. W. Schunk, Ion acceleration in expanding ionospheric plasmas, in *Ion Acceleration in the Magnetosphere and Ionosphere*, *Geophys. Monogr. Ser.*, vol. 38, edited by T. Chang, p. 362, AGU, 1986.
- Sonett, C. P., and D. S. Colburn, The  $SI^+ - SI^-$  pair and interplanetary forward-reverse shock ensembles, *Planet. Space Sci.*, **13**, 675, 1965.
- Wilson, G. R., C. W. Ho, J. L. Horwitz, N. Singh, and T. E. Moore, A new kinetic model for time-dependent polar plasma outflow: Initial results, *Geophys. Res. Lett.*, **17**, 263, 1990.

C. W. Ho, J. L. Horwitz, N. Singh, and G. R. Wilson, Department of Physics and Center for Space Plasma and Aeronomic Research, The University of Alabama in Huntsville, Huntsville, AL 35899.

(Received, August 3, 1992;  
revised February 22, 1993;  
accepted February 12, 1993)

